Rational design of bimetallic catalysts for electrochemical CO_2 reduction reaction: A review

Minhan Li & Jia-Nan Zhang*

College of Materials Science and Engineering, Zhengzhou University, Zhengzhou 450001, China

Received January 21, 2023; accepted March 10, 2023; published online March 28, 2023

The electrochemical CO_2 reduction reaction (eCO$_2$RR) is a compelling approach to convert CO_2 into high-value fuels and chemicals using renewable energies. The rational design of catalysts is of great importance for achieving outstanding performance of this process. Metal-based catalysts have been drawing enormous attention in eCO$_2$RR due to their excellent catalytic performance and flexible selectivity. In the pursuit of overcoming the inherent disadvantages of monometallic catalysts and achieving breakthroughs in the catalytic performance, bimetallic strategy has been receiving extensive concerns and achieving remarkable results over decades. In this review, we attempt to give a comprehensive review on the bimetallic catalysts that are used for eCO$_2$RR. The effects in bimetallic catalysts that contribute to the enhanced eCO$_2$RR performance are first analyzed, demonstrating the superiority of bimetallic strategy. Then, the structural design of bimetallic catalysts is discussed as it plays a key role in eCO$_2$RR. Finally, the current advances and rules of selectivity of bimetallic catalysts in eCO$_2$RR are summarized based on the selectivity behaviors. By reviewing efforts devoted in this field, this review is believed to present a timely overview of the progress of bimetallic eCO$_2$RR catalysts and to offer potential future directions in the aim of developing highly efficient catalysts for eCO$_2$RR.

electrochemical CO_2 reduction, bimetallic catalyst, electronic effect, tandem effect, structural design

1   Introduction

The eCO$_2$RR is a stunning technology and has been advancing rapidly in recent years. This process enables the ambient-condition CO_2 reduction using renewable electric energy for the production of various high-value fuels and chemicals, such as carbon monoxide (CO), formate (HCOO$^-$), methanol (CH$_3$OH), methane (CH$_4$), ethane (C$_2$H$_6$), ethylene (C$_2$H$_4$), ethanol (C$_2$H$_5$OH), acetate (CH$_3$COO$^-$), and n-propanol (n-C$_3$H$_7$OH) [1–3]. The development of efficient catalysts for eCO$_2$RR is central to advance this process, and the reduction products and the catalytic efficiency of eCO$_2$RR are largely dependent on the catalysts used on the cathode. Metal-based

catalysts are the most extensively studied catalysts for eCO$_2$RR, which cover the full range of reduction products of eCO$_2$RR [4,5]. As early as 1980s, Hori and co-workers [6,7] first reported the electrochemical reduction of CO_2 in aqueous solution at different metal electrodes. The metals are classified into for groups according to the major reduction products in eCO$_2$RR, including CO, formate, deep-reduction products (>2 electron transfer), and hydrogen (H$_2$) from competing hydrogen evolution reaction (HER). Since their pioneering work, various metal-based catalysts have been extensively studied for producing specific products in eCO$_2$RR electrodes. After decades of development, metal-based catalysts have been receiving increasing interest and their eCO$_2$RR performance has also been improved greatly. For example, the Faraday efficiencies (FEs) of CO and for-

mate are close to unity on metal catalysts, such as silver (Ag) and bismuth (Bi) [8,9], while the total C_{2+} FE exceeds 80% in alkaline electrolyte or membrane electrode assemble (MEA) system on copper-based catalysts [10].

The mechanism of the eCO_2RR reaction on metal-based catalysts has also been extensively studied by theoretical calculations and spectroscopic techniques [11,12]. The reaction pathway of eCO_2RR involves the transfer of multiple electrons and protons, depending on the products (Figure 1a). The first step for eCO_2RR is the activation of CO_2, which is generally believed to be a concerted-proton-electron-transfer (CPET) process to form adsorbed C_1 species on the surface of catalysts, namely C-bonded *COOH and O-bonded *OCHO intermediates. *COOH is proposed to be the key intermediate for the formation of CO product through the desorption of *CO. Although formate can also form through the desorption of *COOH intermediate, it has been revealed by both experimental and theoretical studies that the production of formate primarily follows the *OCHO intermediate on metal-based catalysts, like tin (Sn), indium (In), and Bi [4,13,14]. The next electron and proton transfer of *CO to *CHO or *COH intermediate is suggested to be critical for the formation of C_1 deep reduction products, including CH_4 and CH_3OH (Figure 1a) [15]. The reaction mechanism of C_{2+} products are much complicated and different pathways are proposed based on theoretical and experimental studies [16–19]. As the major C_{2+} products, C_2H_4 and C_2H_5OH are the most concerned reduction products from eCO_2RR. Based on theoretical calculations by Koper and coworkers [11,20], the lowest energy pathways toward C_2H_4 and C_2H_5OH bifurcate after a common intermediate of *CH_2CHO (Figure 1a).

With the development of metal-based catalysts, the catalytic performance of eCO_2RR has become increasingly limited by the inherent disadvantages of monometallic catalysts. Firstly, to achieve high-efficiency eCO_2RR, noble-metal catalysts are often required, such as gold (Au) and palladium (Pd), which exhibit outstanding CO and formate production at low overpotential, respectively [21,22]. The use of noble metals as monometallic catalysts for eCO_2RR undoubtedly increases the cost and undermines the competitiveness of this process. As for deeper reduction products with higher value, there are a few options of noble metals, as Cu is the only one that can reduce CO_2 to deeper reduction products with decent activity and selectivity [3,23]. However, Cu-based catalysts still suffer from diverse reduction products, high overpotential and severe HER competition [24]. Secondly, eCO_2RR involves multi-step reactions and a variety of intermediates. The scaling relationship among intermediates hinders the acquisition of high activity and selectivity during eCO_2RR and imposes substantial overpotentials for the conversion of CO_2 to different products [25]. Numerous studies have shown that breaking scaling
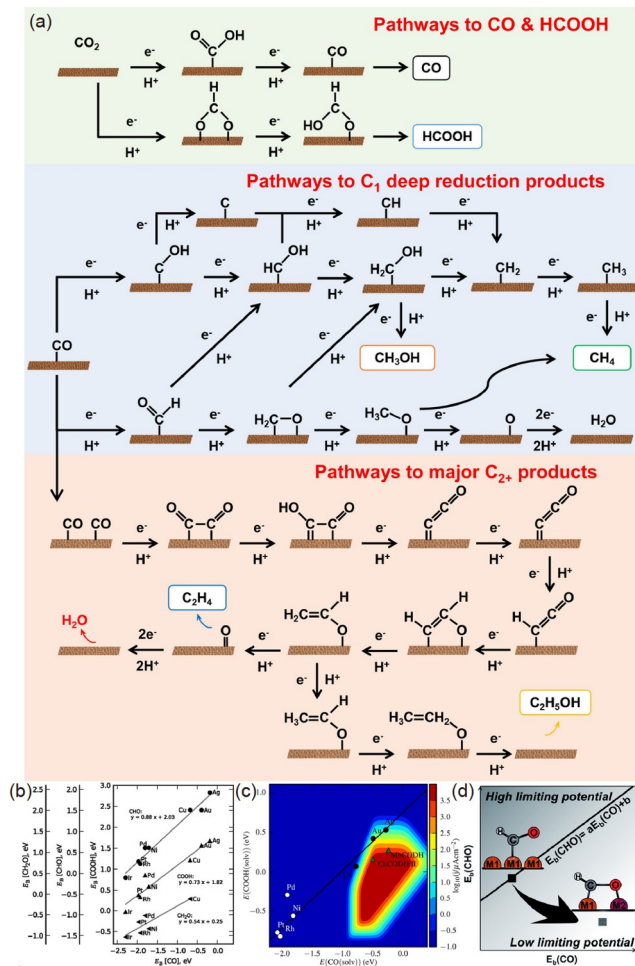

Figure 1   (a) The proposed reaction pathways of eCO_2RR to various products. (b) The scaling relationship of adsorption energies of carbon-bonded adsorbates in eCO_2RR. Reproduced with permission from [28]. Copyright 2012, American Chemical Society. (c) The kinetic activity calculation of CO_2-to-CO conversion on metals and enzymes based on adsorption energies of *CO and *COOH. Reproduced with permission from [25] Copyright 2013, American Chemical Society. (d) Schematic illustration of the decoupling of scaling relations between *CHO and *CO to lower the limiting potential. Reproduced with permission from [29]. Copyright 2020, The Royal Society of Chemistry (color online).

relationship is a promising way to improve the catalytic performance of eCO_2RR [26–28]. The scaling relationship is universal for intermediates during eCO_2RR due to the similar chemical bonds between adsorbed species and catalyst surfaces, such as *CO, *COOH, and *CHO (Figure 1b) [11]. Taking CO as an example, an excellent CO_2-to-CO catalyst should have a strong adsorption of *COOH and a weak adsorption of *CO. However, limited by the scaling relationship, such binding strengths of *COOH and *CO are hardly to be obtained simultaneously on monometallic catalysts.

Bimetallic catalysts have been utilized for eCO_2RR since 1991 and have arousing growing concern [30,31]. Why bimetallic catalysts are highly desired and suitable for eCO_2RR? Firstly, it is possible to break the scaling relationship and thus improve the energy efficiency and the selectivity of

specific products by bimetallic strategy [32]. In nature, carbon monoxide dehydrogenase is able to convert CO_2 into CO with a high turnover frequency at ultralow overpotentials [33]. Such a superior catalytic performance is believed to deviate the scaling relationship between *COOH and *CO by comprising Ni and Fe functional sites (Figure 1c) [25]. Inspired by nature, bimetallic catalysts could also possess bifunctional active sites to break the scaling relationship in eCO_2RR due to the introduction of heteroatoms (Figure 1d) [34]. Therefore, the designing of interface or atomic arrangement in bimetallic catalysts holds great promise to lower the overpotential and tune the selectivity for eCO_2RR. Secondly, bimetallic strategy is an efficient way to tune the electronic structure of active sites, which largely determines the interaction between adsorbed intermediates and catalyst surface. For instance, d-band theory has been widely used to describe the adsorption of intermediates on transition metals. The change in d states is closely related to the bonding behaviors between transition-metal surfaces and adsorbates [26]. Thereby, the activity and selectivity of eCO_2RR can be enhanced by bimetallic strategy through the tuning of binding energy of intermediates [35]. Thirdly, alloying is an efficient approach to reduce the usage of noble metals and boost the mass activity [36]. The bimetallic catalysts with noble-metal shells or overlayers have been demonstrated to be outstanding candidates in various electrocatalysis processes [37–39]. Noble metals, such as Au, Pd, and Ag, exhibit great eCO_2RR activity and selectivity at low overpotentials. Alloying them with earth-abundant metals is a promising way to minimize the usage of noble metals and greatly increase the mass activity [40,41].

Previously, several reviews that involve the application of bimetallic catalysts in eCO_2RR have been published, focusing on the catalytic performance of bimetallic catalysts in eCO_2RR [42], the Cu-based or Pd-based bimetallic catalysts [2,43,44], and the compositional survey [45]. Up to now, various bimetallic catalysts with different structures and atomic patterns have been developed for eCO_2RR (Scheme 1). However, a systematic summary with regard to the advantages, rational design, and the laws of selectivity of bimetallic catalysts for eCO_2RR is still lacking. Therefore, the aim of this review is to take a comprehensive summary at the research status of bimetallic catalysts for eCO_2RR, including the promotion effects, the structural design, and the advances of bimetallic eCO_2RR catalysts. After that, the urgent issues and the potential future directions in this area are proposed in hopes of advancing the design of efficient bimetallic catalysts and the development of eCO_2RR.

2   The effects of bimetallic catalysts for eCO_2RR

2.1   Electronic effect
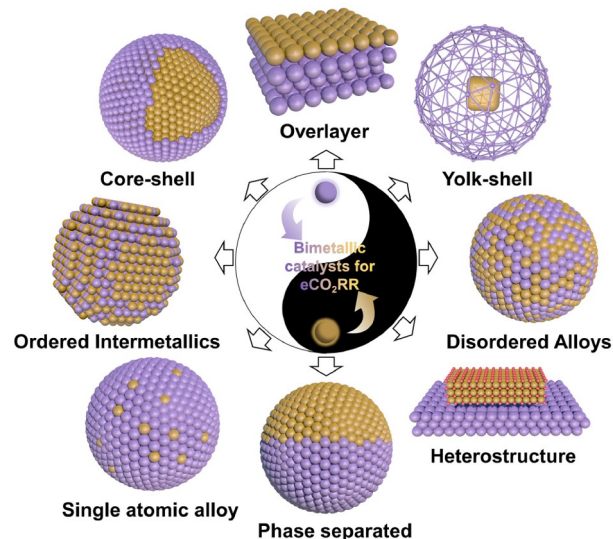
Scheme 1   Schematic illustration of bimetallic catalysts with different structures for eCO_2RR (color online).

Electronic properties of catalysts are probably the most important factor that determines the catalytic performance in reactions. The electronic effect significantly changes the energy levels, the carried charge, the orbital occupancy, and the magnetic property of the active sites on the surface of catalyst, thereby affecting the hybridization and charge transfer between active sites and adsorbates [46]. For transition metals, their d-band structure is often concerned as the interactions between their d bands and the adsorbate determines the binding strength. The regulation of electronic properties in catalysts can be achieved by various approaches, among which bimetallic strategy is an experimentally proven and extensively adopted method for catalysis [47]. In bimetallic catalysts, the electronic effects are usually brought by the changed coordinated atoms or the altered bond length. The former is referred as the ligand effect and the latter is known as the strain effect. Therefore, the electronic effect in bimetallic catalysts is a common and effective way to boost the catalytic performance of eCO_2RR by tuning the binding energy [47–49].

2.1.1   Ligand effect

Different from monometallic catalysts, the change of surrounding coordinated metal atoms in bimetallic systems gives rise to the distinct electronic structures and catalytic performance, which is known as the ligand effect [50]. Driven by the differences in the electronegativity and the filling state of valence band between the combined metals, a specific electron transfer occurs through the heteronuclear metal–metal bond formed on the bimetallic surface [51]. As a result, each constituent in bimetallic systems exhibits a drastic change in the electronic properties and catalytic performance [52]. For transition-metal-based catalysts that

are widely used in eCO$_2$RR, the ligand effect in the bimetallic catalysts influences the states of d-band, which determines the binding strength with the adsorbates [47]. Due to the scaling relationship between *COOH and *CO, a balance between the binding strength of *COOH and *CO is needed for improving the CO$_2$-to-CO activity. Therefore, it has been reported that the ligand effect played a predominant role in determining the d-band center of Au–platinum (Pt) bimetallic catalyst, which governed the binding strength of adsorbates (Figure 2a) [53]. Similarly, alloying Cu with Au was proposed to efficiently adjust the d-band center relative to the Fermi level. The great correlation between the downshifted d-band center and the weakened binding strength of *CO strongly suggested that electronic effect was the main reason for the enhanced CO production on Au–Cu alloy catalysts (Figure 2b) [54]. Kim and co-workers [55] verified the charge transfer from Cu core to thin layer Au skin by the shifted XPS Au 4f peak and the changed valence band spectra, which suggested an altered electronic structure and endowed a favorable d-band center shift for eCO$_2$RR to CO. Toshihiro and co-workers [56] modified Pd nanoparticles with controllable Cu layers by the under-potential deposi-

tion. The charge transfer from Pd to Cu downshifted the average d-band center away from the Fermi level, which weakened the CO adsorption strength and improved the CO tolerance for enhanced CO selectivity and catalytic stability. Jeon and co-workers [57] revealed that upon the reduction of ZnO under the eCO$_2$RR condition, the CuZn alloy formed gradually and thus the ligand effect increasingly became prominent, which shifted the d-band center of Cu and deviated from the original selectivity. Apart from the modification of d-band states, the work function, which describes the energy for removing one electron out of catalyst surface in the vacuum, can also be tuned in bimetallic catalysts. The work function decreased 4.55 eV of pure Cu to 4.50 eV, 4.46 eV, and 4.16 eV of Cu$_3$Zn, CuZn, and CuZn$_3$ bimetallic catalysts (Figure 2c). The decreased work function facilitated the activation of CO$_2$ and accelerated the kinetic of eCO$_2$RR [58]. Recently, Liu and co-workers [59] found that the significant delocalization of p orbital of Bi induced by electronic interaction at Cu–Bi interface enhanced the binding strength of *OCHO or *COOH and lowered the energetic barrier for the formate formation (Figure 2d). In short, as a way of the regulation of electronic structure, the ligand effect
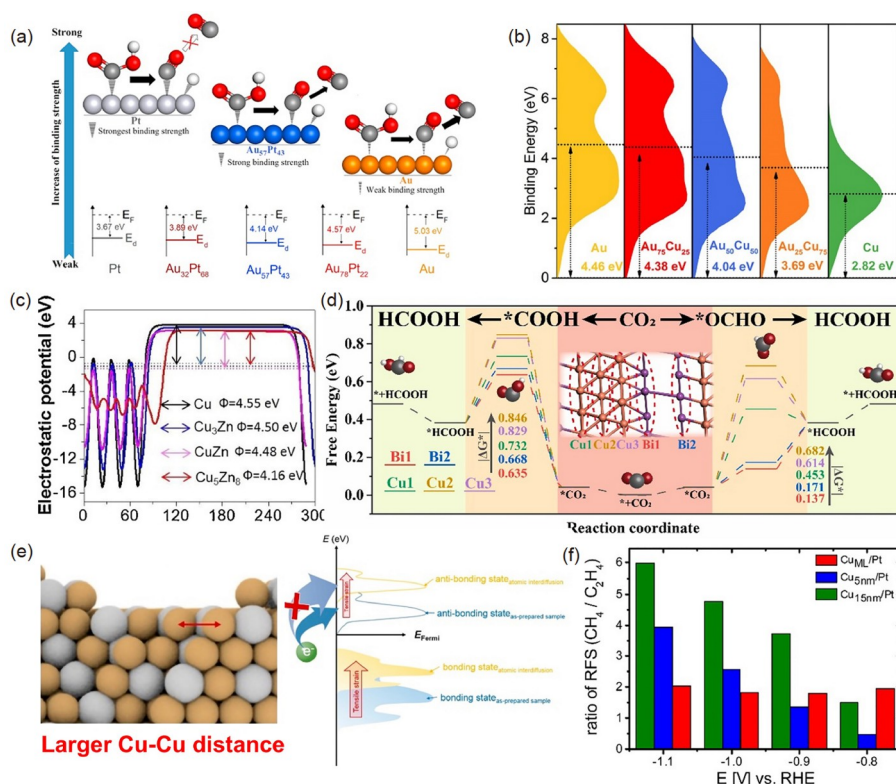

Figure 2   Electronic effects in bimetallic catalysts. (a) Schematic illustration of binding strengths of *COOH, *CO and *H intermediates on Au–Pt bimetallic catalysts as a function of the d-band center position. Reproduced with permission from [53]. Copyright 2017 Elsevier. (b) d-band states of Au, Cu, and Au–Cu alloys determined by surface valence band X-ray photoemission spectra. Reproduced with permission from [54]. Copyright 2019, American Chemical Society. (c) Calculated electrostatic potentials and work functions of Cu and CuZn alloys. Reproduced with permission from [58]. Copyright 2020 Elsevier. (d) The free energies for the formate formation on different Cu–Bi sites. Reproduced with permission from [59]. Copyright 2022 Elsevier. (e) Schematic illustration of the enlarged Cu–Cu distance caused by interdiffusion of Ag and Cu atoms (left) and the changes in binding states between adsorbate and metal (right). Reproduced with permission from [64]. Copyright 2020, American Chemical Society. (f) Selectivity ratios for CH$_4$/C$_2$H$_4$ on Cu layers with different thicknesses deposited on the Pt substrate. Reproduced with permission from [68]. Copyright 2013, American Chemical Society (color online).

tunes the electronic states of the active sites through the electronic interaction with neighboring coordination atoms in bimetallic catalysts and thus plays an important role in interacting with intermediates in eCO$_2$RR, such as *COOH, *CO, *OCHO, and *HCCOH [47].

2.1.2 Strain effect

The strain effect is another effective and common strategy to influence the electronic structure of active sites in bimetallic catalysts. Elastic strain is a fundamental physical property existing in solid materials. The lattice mismatch between metals can stretch or contract the distance between surface atoms, causing either tensile or compressive lattice strain on bimetallic catalysts. The strain strategy has been extensively adopted to modulate the electronic properties at the surface and the reaction energetics of electrocatalysts. Experimentally and theoretically, the shifted d-band centers caused by strains have been confirmed in different bimetallic systems, such as Pt–Cu and Cu–Au [37,60], which significantly altered the interaction between strained surfaces and the adsorbates. Theoretically, it has been revealed that the tensile strain on Cu surface decreased adsorption energies of initial, transition, and final states during the *CO dimerization, and thereby was expected to increase the coverage of *CO and facilitate the CO–CO coupling [61]. For the bimetallic catalysts, it was found that the incorporation of heteroatoms with different radius, such as Au and Sn, in Cu caused increasing microstrains in bimetallic catalysts, which changed the adsorption energetics of intermediates and improved the kinetic of interfacial electron transfer for eCO$_2$RR [54,62]. Clark and co-workers [63] found that surface alloying with random Ag substitution formed with proper Ag doping, although Cu and Ag are immiscible in bulk. Given the similar electronegativity but different atom radius between Ag and Cu, it was believed that the randomly incorporated Ag atoms on the surface triggered the compressive strain, which changed the electronic structure and affinity to H and O atoms of Cu. Similarly, Chang and co-workers [64] reported that the alloying process between Cu and Ag on the Cu$_{68}$Ag$_{32}$ catalyst surface was driven by dynamic reoxidation–reduction cycles. With the continuous formation of surface CuAg alloy, the tensile strain was caused by the difference in lattice parameters of Ag and Cu. The enlarged Cu–Cu bond shifted the d-band center toward Fermi level, which elevated energy of the antibonding and thus strengthened the binding strength of the key intermediate for CH$_4$ (Figure 2e).

The bimetallic catalysts with core–shell and overlayer structures are frequently used for eCO$_2$RR, through which the strain effect can be introduced for regulating electronic properties and enhancing catalytic performance. It is known that the ligand effect is highly dependent on neighboring coordinated atoms and largely vanishes across atoms, while the influence of the strain effect often spans several layers of

atoms [65]. Therefore, through the control of the thickness of the shell or overlayer, it not only enables the decoupling of strain and ligand effects in bimetallic catalysts, but also realizes the fine tuning of surface electronic properties and catalytic performance [37,39]. For instance, the SnO$_2$ shell on the Cu core with a thickness of 0.8 nm was proposed to be critical for the high CO Faradaic efficiency, which mainly resulted from the lattice compression and Cu doping [66]. Monzó and co-workers [67] reported Au@Cu core–shell nanoparticles for eCO$_2$RR and found that the H$_2$ and CH$_4$ production increased at the expense of decreased C$_2$H$_4$ with the thickness of Cu layers. Similarly, the selectivity between CH$_4$ and C$_2$H$_4$ on the Pt-supported Cu overlayer was found to be well correlated to the thickness of the deposited Cu overlayer, demonstrating the strain effect was able to tune the adsorption of intermediates and alter the reaction pathways for eCO$_2$RR (Figure 2f) [68]. In summary, the influence of the strain on the electronic structure on bimetallic catalysts can be tuned by both the category and the extent of exerted strain. Therefore, taking advantage of the strain effect in bimetallic catalysts for eCO$_2$RR is a promising way to boost the catalytic performance and uncover the electronic structure–activity relationship. In this way, it is possible to modulate the binding energies of different adsorbed intermediates concurrently. However, it may be difficult to achieve the best catalytic performance due to the scaling relationship that still remains in bimetallic catalysts with the predominant electronic effect.

2.2 Geometric effect

The geometric effect in bimetallic catalysts is usually correlated to the surface atomic arrangement. The adsorption energy of different intermediates on adsorption sites on the surface of bimetallic catalysts can be tuned through the composition of individual or ensemble of metal atoms that serve as the adsorption sites. Therefore, this effect related to the ensemble of surface atoms on bimetallic catalysts is also referred as the ensemble effect [50,69]. Ma and co-workers [70] reported that the geometric effect brought by the atomic arrangement of Cu and Pd played a key role in the selectivity of eCO$_2$RR on Cu–Pd bimetallic catalysts, on which a broad range of C$_1$ and C$_2$ reduction products could be selectively produced (Figure 3a). Li and co-workers [71] studied the eCO$_2$RR on the bimetallic Ag–Cu catalyst and suggested that incorporating Ag atoms on the Cu surface enriched the geometry of surface binding sites. Theoretically, the type of binding sites on Cu(111) increased from 4 to 16 by one Ag atom substitution on Cu(111) surface (Figure 3b). As such, the different surface atom ensembles that made up the binding sites for intermediates undermined the highly coordinated nature of Cu surface and favored the ethanol pathway. Theoretical calculation has revealed that sub-
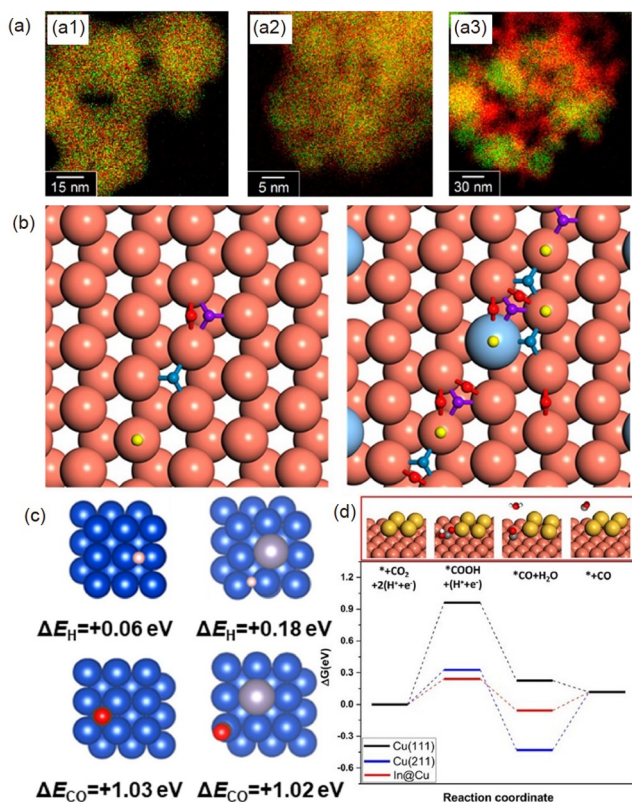
Figure 3 Geometric effects. (a) The EDS elemental maps of Cu (red) and Pd (green) for bimetallic Cu–Pd catalysts with different atomic mixing patterns: ordered (a1), disordered (a2), and phase-separated (a3). Reproduced with permission from [70]. Copyright 2017, American Chemical Society. (b) Binding site configurations for Cu and Ag/Cu catalysts. Reproduced with permission from [71]. Copyright 2019, American Chemical Society. (c) Optimized geometries and relative energies of H and CO adsorbed on the Cu (100) facet and Sn-modified Cu(100) facet. Reproduced with permission from [72]. Copyright 2016, American Chemical Society. (d) Free-energy diagrams for the CO_2-to-CO conversion on Cu (111), Cu (211), and In@Cu surfaces. Reproduced with permission from [73]. Copyright 2018, American Chemical Society (color online).

stituting Cu atoms on Cu(100) and Cu(111) surfaces by Sn dismantled the H adsorption sites and increased the H adsorption energy, which disfavored the competing H_2 production in eCO_2RR. However, the adsorption of CO was almost undisturbed by the Sn substitution, which accounted for the enhanced CO FE on the Cu–Sn bimetallic catalyst (Figure 3c) [72]. As the key intermediates for the CO production from eCO_2RR, the scaling relationship between C-bonded *CO and *COOH hampers the efficiency of CO_2-to-CO. DFT study has suggested that the strong scaling relationship between *CO and *COOH intermediates can be mitigated by stabilizing *COOH through the introduction of additional sites that bond end O atoms [25]. Luo and co-workers [73] suggested that the introduction of more O-affinitive indium (In) metal on Cu provided the additional O bond for stabilizing the *COOH intermediate at the Cu–In interface, where the geometric effect rather than electronic effect was proposed to play a primary role in the high CO FE

obtained on the CuIn20 catalyst (Figure 3d). Similarly, Zn metal sites in the Ag–Zn alloy catalyst was proposed to act as oxophilic sites, which stabilized the *CHO intermediate by forming a bidentate configuration. As expected, much enhanced methane and methanol production was obtained on the Ag–Zn alloy [74]. Through the geometric effect, diverse binding sites can be introduced on the bimetallic catalyst surface, and the different binding configuration for adsorbed intermediates can be realized. In this way, the adsorption energy of the certain intermediate may be tailored independently. Therefore, the geometric effect in bimetallic catalysts is a promising way to break the scaling relationship between intermediates and increase the selectivity in eCO_2RR.

2.3 Tandem effect

Upgrading simple molecular blocks, CO_2, into complex products involves multiple steps of the bond breaking and formation. Ideally, each step may require different active sites to proceed with the optimal energy barrier. Inspired by the complex reactions catalyzed by enzymes occurring spatially and temporally in biological systems, the conception of tandem catalysis has been put forward and widely used in heterogeneous catalysis [75]. It is known that multiple reaction steps and different intermediates are involved in eCO_2RR. Therefore, the concept of tandem catalysis that realizes the overall reaction step-by-step in sequence at different active sites holds great promise for improving eCO_2 RR performance, especially for Cu-based catalysts [76], which is also referred as sequential catalysis or relay catalysis [77–79]. Generally, *CO is believed to be the key intermediate for the further reduction of CO_2 to deep reduction products in eCO_2RR. For instance, the hydrogenation of *CO to *CHO is reported to be critical for CH_4 production, while the coupling of *CO with another C_1 intermediate is regarded as the prerequisite for C_{2+} products. Therefore, the tandem effect has been widely adopted on bimetallic catalysts containing Cu to improve the activity of deep reduction products in eCO_2RR. To achieve this goal, it has been proposed that the local concentration and coverage of *CO intermediates plays an important role in the reaction pathways, the C–C coupling, and the suppression of HER [61,80,81]. Therefore, it is reasonable to combine CO-producing active sites with Cu sites to take advantage of the tandem effect for eCO_2RR, such as Cu–Zn [82], Au–Cu [78,83], and Cu–Ag [84,85].

The key for the deployment of the tandem effect relies on the transfer of generated *CO from the original site to neighboring Cu sites for the further reduction, which is known as CO spillover [86]. Based on the theoretical calculations, the CO spillover from Ag or Au sites to Cu sites was found to be thermodynamically and kinetically favorable. Zhang and co-workers [84] demonstrated that ~70% of

the CO produced on Ag could migrate to the Cu surface and further be reduced to CH_4 at the optimal Cu coverage on the Ag surface by precisely controlling the surface coverage of deposited Cu on the Ag foil and carefully comparing the activity trends. Furthermore, the CO transfer was suggested to surmount a length scale up to micron-scale [77]. Through the fabrication of a micropattern system consisting of Au or Ag in close proximity to Cu, it has been proved that a substantial portion of the generated CO was able to transport across micron-scale and further consumed on Cu, depending on the Cu area coverage (Figure 4a) [77].

The *CO spillover may proceed through two possible ways: (1) CO generated on CO-producing sites desorbed and is then captured by Cu to continue further reaction; (2) *CO intermediates directly diffuse through the interfaces between CO-producing and Cu sites. Gao and co-workers [86] reported that the efficient CO spillover through the second way was the main reason for the enhanced activity and selectivity toward CO_2-to-C_2H_4 conversion on CuAg bimetallic catalysts. The efficiency of the CO spillover based on specific TOF was calculated to be more than 95%. Namely, ~95% of the CO produced on Ag sites spillover to Cu and was further reduced on Cu sites. This concept has been validated by the much-enhanced population of intermediates detected by

operando Raman spectroscopy on CuAg catalysts, such as *CO and CH-containing intermediates (Figure 4b).

The influence of the tandem effect of bimetallic catalysts on the performance of eCO₂RR can be mainly understood from two aspects. On one hand, it has been reported that the spillover of *CO may facilitate the C–C coupling through the insertion mechanism [87,88]. Ren and co-workers [89] suggested that the CO produced on Zn could transfer from Zn to Cu sites and be inserted in adsorbed *CH₂ intermediates to form C_2H_5OH on Cu_4Zn bimetallic catalysts. On the other hand, through the CO spillover, the increased local CO concentration has been detected and reported on various bimetallic catalysts, which is important for the further reduction of CO and C–C coupling [90]. As evidenced by modeling, the local CO concentration around Cu may break the limit of CO solubility by CO spillover from nearby Au sites [77,91]. Theoretically, it has been reported that the energy barrier for *CO coupling could be lowered by increasing *CO coverage [61], while the pathways to C_2H_4 and C_{2+} oxygenate products exhibited the inverse dependency on *CO coverage [81]. Experimentally, the improved local CO concentration is believed to account for the increased C_{2+} production in eCO₂RR. Morales-Guio and co-workers [91] fabricated Au nanoparticles on Cu and attributed the en-
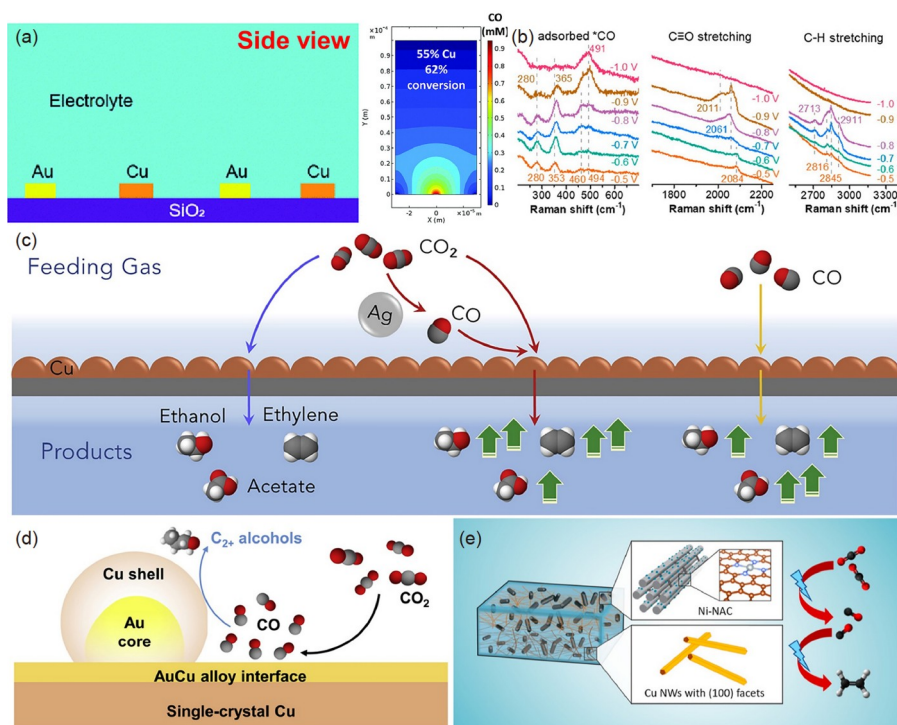

Figure 4 Tandem effects in bimetallic catalysts. (a) Schematics of interdigitated bimetallic electrodes (left) and the calculated CO concentration contours and conversion of over-spilled CO for interdigitated devices with Cu coverage of 55% (right). Reproduced with permission from [77]. Copyright 2018, The Royal Society of Chemistry. (b) *Operando* Raman spectroscopy of CuAg catalysts. Reproduced with permission from [86]. Copyright 2019, American Chemical Society. (c) Schematic illustration of the tandem catalysis for eCO₂RR (red route) *versus* traditional eCO₂RR (blue route) and CO reduction reaction (yellow route). Reproduced with permission from [92]. Copyright 2020 Elsevier. (d) The schematic diagram of tandem electrocatalysis pathway on the reconstructed Au–Cu electrode. Reproduced with permission from [94]. Copyright 2022 Elsevier. (e) Schematic illustration of Cu/Ni-NAC hybrid catalyst for tandem catalysis. Reproduced with permission from [95]. Copyright 2022, American Chemical Society (color online).

hanced CO_2-to-C_{2+} alcohols performance to the tandem catalysis mechanism. Chen and co-workers [92] decoupled the CO_2-to-C_{2+} steps and verified the tandem strategy at high reaction rate by physical mixture of Cu and Ag nanopowders. The lack of the interaction and interface between Cu and Ag exclude other effects in bimetallic catalysts. The tandem catalysis of CO produced on Ag and C–C coupling on Cu contributed to a high-rate C_{2+} production. The increase of C_{2+} through the tandem effect obtained on integrated Cu–Ag nanopowder catalyst layers was even higher than the eCO_2RR performance of pure CO-feeding on Cu alone, demonstrating the unique mechanism beyond the CO enrichment by the tandem effect in bimetallic catalysts (Figure 4c).

Recently, the studies of the tandem effect for enhanced eCO_2RR performance have become a hotspot in this field. A novel Au@Cu_2O bimetallic catalyst with a yolk–shell structure was proposed to serve as a tandem nanoreactor, where moderate CO coverage could be tuned to maximize CH_4 production [93]. Zhu and co-workers [94] reported an epitaxial Au–Cu bimetallic heterostructure, which exhibited reduced onset potential for C_{2+} alcohols and drastically increased ratio of C_{2+} alcohol to hydrocarbons. Under the practical eCO_2RR condition, a dynamic restructuring led to a reconstructed bimetallic system consisting of Au–Cu alloy support and Au@Cu core–shell nanoparticles, by which a tandem mechanism was proposed to boost CO_2-to-C_{2+} alcohols (Figure 4d). Apart from traditional CO-producing metals, single-atom catalysts (SACs) containing nitrogen-coordinated transition metals, such as Fe, Co, and Ni, have exhibited excellent CO_2-to-CO activity and selectivity in eCO_2RR [1]. Therefore, the design of tandem catalysts consisting of transition-metal-based SACs and Cu has also been developed recently, such as the combination of Ni-SACs with Cu nanoparticles and nanowires (Figure 4e) [95,96]. In summary, the tandem effect of bimetallic catalysts is a promising strategy for improving activity and selectivity toward hydrocarbons and oxygenates in eCO_2RR as multiple steps and intermediates are involved. To bring the efficiency of tandem effect into full play, the design of bimetallic catalysts demands appropriate ratio and elaborate spatial distribution of different active sites for sequential reaction steps.

2.4   Synergy of different effects

In fact, both electronic and geometric effects play important roles in the activation and adsorption of intermediates in eCO_2RR. The electronic effect regulates the electronic structure of adsorption sites, while the geometric effect is capable of breaking scaling relationship between intermediates. To achieve high efficiency CO_2-to-CO conversion, it has been suggested that electronic and geometric effects were necessary to enhance the binding strength of *COOH

and deviate the scaling relationship between *COOH and *CO [53]. In many cases of bimetallic catalysts, these two effects work synergistically and are hard to be distinguished from each other [50]. For instance, the strain caused by heteroatom doping is inevitably accompanied by the electronic perturbation in bimetallic catalysts, and the compressed or tensile metal bond is also related to the altered surface geometry and thus is also referred as a geometric effect [37]. Therefore, the synergistic effect that integrates the advantages from different effects in bimetallic catalysts may collaboratively increase the efficiency of eCO_2RR process. It has been demonstrated by theoretical studies where Cu monolayers loaded on the Au substrate could facilitate C–C coupling through tensile strain and electron transfer [97]. Kim and co-workers [47] studied the synergy between geometric and electronic effects for eCO_2RR on Au–Cu bimetallic catalysts. It was found that the electronic effect alone cannot fully explain the activity volcano obtained on Au–Cu catalysts with different composition. The Au_3Cu catalyst that exhibited the highest CO_2-to-CO activity was suggested to benefit from the geometric effect as well, where the geometric effect on the surface with uniform and random atomic arrangement help stabilize the *COOH intermediates by adjacent Cu atoms to Au (Figure 5a). Wang and co-workers [98] reported that the Ag doping in Cu gave rise to an asymmetric C–C coupling active site that consisted of two neighboring Cu sites with different electronic properties. This asymmetric Cu–Cu site was generated by both ligand and strain effects of Ag doping, which collaboratively contribute to the decrease of activation energy required for C_1–C_1 and C_1–C_2 coupling in eCO_2RR (Figure 5b). Chu and co-workers [99] suggested that the high CO FE obtained on the CuO–In_2O_3 bimetallic catalyst was ascribed to the synergy between electronic and geometric effects. The Cu sites with enhanced electron density and the oxophilic In_2O_3 species at the interface jointly strengthened the adsorption of *COOH intermediates. Ma and co-workers [100] prepared self-supported nanoporous $AuCu_3$@Au with a core–shell structure by selectively etching the monolithic AuCu alloy ribbons. The stability of *COOH intermediates was improved by the double-dentate adsorption configuration and favorable electronic structure on the $AuCu_3$@Au alloy catalyst, which contributed to high eCO_2RR performance at the low overpotential. Recently, the similar combination of electronic and geometric effects for stabilizing *COOH was also reported on the Zn–Cu bimetallic catalyst [101]. Cui and co-workers [102] reported that the strong interaction between Ag and Pd reshaped the d band of Pd, while the incorporation of Ag atoms disrupted the multifold CO binding sites on the Pd surface. As a result, the strong CO bonding on Pd was mitigated by alloying with Ag through ligand and ensemble effects (Figure 5c). Although different effects in bimetallic catalysts are complex and intricate, the contribu-
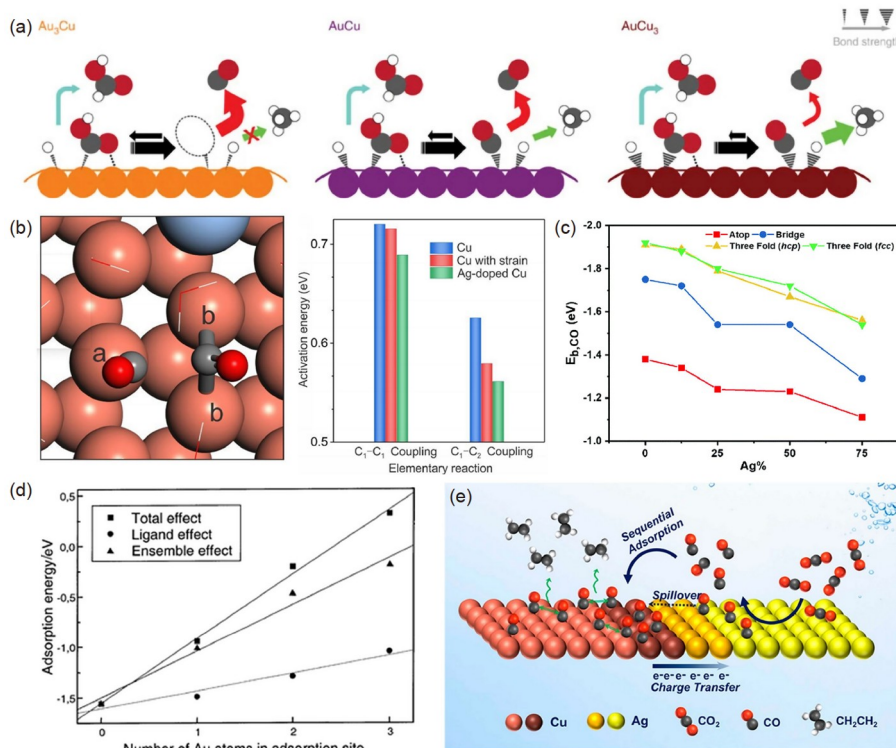
Figure 5 Synergistic effects. (a) Schematic showing the proposed mechanism for eCO$_2$RR on the catalyst surface of Au–Cu bimetallic nanoparticles. Reproduced with permission from [47]. Copyright 2014, Springer Nature. (b) Two types of neighbouring Cu atoms labeled as a and b on Ag-doped Cu surface (left) and activation energies of C$_1$–C$_1$ and C$_1$–C$_2$ coupling on Cu, Cu with strain, and Ag-doped Cu (right). Reproduced with permission from [98]. Copyright 2019, Springer Nature. (c) Calculated CO adsorption energies at the different Pd sites on AgPd alloys with varying Ag concentrations. Reproduced with permission from [102]. Copyright 2020, The Royal Society of Chemistry. (d) Contribution of the ligand and ensemble effects to CO adsorption on hollow sites of Au/Pd(111). Reproduced with permission from [50]. Copyright 2001, The Royal Society of Chemistry. (e) Schematic illustration of the proposed mechanism for C$_2$H$_4$ production through the synergy of tandem and electronic effects in the Ag–Cu NDs. Reproduced with permission from [104]. Copyright 2019, American Chemical Society (color online).

tion of individual effect to the changed interaction with adsorbates is different [103], and is related to the surface structure of the catalyst. It has been revealed by DFT calculation that ligand and ensemble (geometric) effect worked together to tune the CO adsorption on the hollow sites of Au/Pd(111). The result demonstrated that the ensemble effect caused by the Au substitution in the threefold adsorption sites on Pd(111) prevailed over the ligand effect (Figure 5d) [50]. The tandem and electronic effects have also been reported to synergistically boost the increased C$_2$H$_4$ activity and selectivity. The Au–Cu nanodimer with tunable interface was designed, by which the flux of CO produced on Ag domains to Cu domains increased the C$_2$H$_4$ FE through the tandem mechanism. Further, due to the large interface, the electron transfer from Cu domain to Ag domain decreased the electron density of Cu in Au–Cu nanodimers, which also strengthened the binding of CO and facilitated C–C coupling (Figure 5e) [104]. Based on the above discussion, it is clear that different effects collaboratively contribute to eCO$_2$RR activity and selectivity on bimetallic catalysts. On one hand, the eCO$_2$RR studies on bimetallic model catalysts with well-designed structure are needed to disentangle the different

effects in bimetallic catalysts. On the other hand, it should be noted that these effects may be conflicting in a bimetallic catalyst. To optimize the eCO$_2$RR performance, it is reasonable to effectively integrate the advantage of various effects in bimetallic catalysts.

The major effects in bimetallic catalysts which contribute to eCO$_2$RR performance are illustrated and discussed. Undoubtedly, the deployment of bimetallic catalysts is a promising strategy for eCO$_2$RR, while the function and efficiency of bimetallic effects are largely dependent on the structure of bimetallic catalysts, such as the component allocation, the spatial arrangement, the atomic mixing pattern, and the conjunction boundary of the combined metals. Therefore, the elaborate design of the structure is highly desired and will be discussed in the next section.

3　Structural design of bimetallic catalysts for eCO$_2$RR

As discussed in Section 2, the various effects of bimetals are largely dependent on the structure and atomic arrangement.

For example, ligand and strain effects (electronic effects) often show great influence on the bimetallic catalysts with the core–shell or overlayer structure, while the geometric effects may have greater influence on the alloy surface where the two metals are evenly mixed. As for heterostructures, the geometric or tandem effect at the interfaces often plays an important role. To make full use of bimetallic catalysts to promote the activity and selectivity of eCO$_2$RR, the elaborate design of structure and mixing pattern is necessary [5].

3.1   Core–shell structure

The bimetallic catalysts with core–shell structure are widely studied for eCO$_2$RR, which consist of an inner core and an outer shell with different structure and component [105]. One of the fascinating advantages of core–shell structure is to reduce the usage of noble metals and increase the mass activity. Dai and co-workers [41] reported a high CO FE of 94% and CO mass activity of 439 mA mg$_{Au}^{-1}$ obtained on a Cu@AuCu core–shell catalyst, which significantly outperformed the pure Au due to the low Au content of 17% in the alloyed AuCu shell (Figure 6a). Sun and co-workers [40] suggested that an Au–Fe core–shell catalyst consisted of an Au shell and an Au–Fe alloy core derived from Fe leaching under electrocatalysis. At low overpotential, the Au–Fe catalyst exhibited a ultrahigh mass activity of 48.2 mA mg^{-1}, which was nearly 100 times higher than that of Au counterpart (Figure 6b).

Through the construction of core–shell structure, various favorable effects can be introduced to bimetallic catalysts for eCO$_2$RR. A combination of strain and ligand effects are often suggested to increase the activity and regulate the selectivity in eCO$_2$RR on the metal overlayer, such as Cu/Pt and Pd/Cu [56,68,106], which is a variation of core–shell structures. The doping of core metal in the shell region and the surface strain caused by the core jointly contribute to the variation of activity and selectivity of bimetallic catalysts in eCO$_2$RR. Therefore, the shell component and thickness in core–shell bimetallic catalysts are critical for eCO$_2$RR. The thickness of the SnO$_2$ shell was found to play an important role in determining the main reduction product in eCO$_2$RR. The thin SnO$_2$ shell (0.8 nm) facilitated the formation of CO due to the compressive strain and Cu infiltration, while the thick one (1.8 nm) exhibited a Sn-like activity with the formate as the main product (Figure 6e) [66]. The optimal SnO$_x$ shell of ~1.7 nm was suggested to be favorable for the stabilization of *OCHO *via* the strain effect caused by Ag–Sn bimetallic cores [107]. Similarly, the precise control of the Ag or Pb layer over the Cu nanocore was also reported to be critical for enhancing the production of C$_2$H$_4$ and C$_{2+}$ liquid products, respectively [108,109]. On the other hand, the core–shell structure contains different active sites and provides spaces or interfaces for reactions to proceed in sequence, which is a
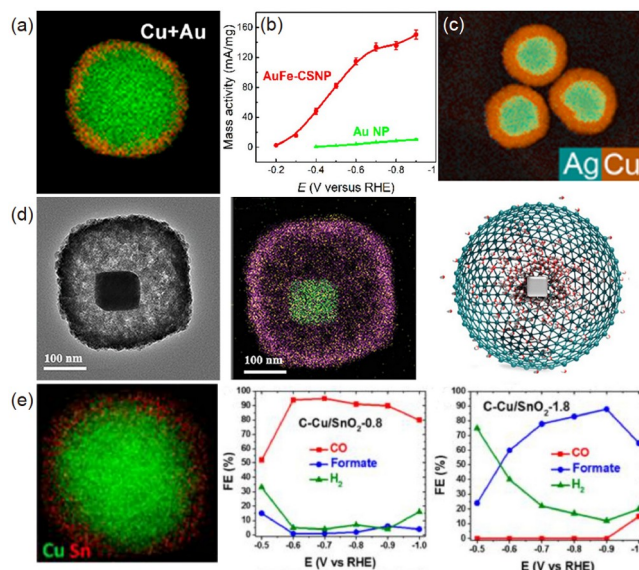

Figure 6 Core–shell structure bimetallic catalysts. (a) EDS elemental maps showing the distribution of Cu and Au in Cu@AuCu catalysts. Reproduced with permission from [41]. Copyright 2021, American Chemical Society. (b) The mass activity of AuFe bimetallic catalysts and Au NPs. Reproduced with permission from [40]. Copyright 2017, American Chemical Society. (c) EDS elemental mapping images of Ag@Cu-p2.8 catalyst. Reproduced with permission from [110]. Copyright 2022, American Chemical Society. (d) EDX mapping images of yolk–shell Ag@Cu$_2$O catalyst and schematic diagrams showing the CO flux in Ag@Cu$_2$O. Reproduced with permission from [93]. Copyright 2021, John Wiley & Sons, Inc. (e) EELS elemental mapping of Cu/SnO$_2$ NPs and potential dependent FEs on Cu/SnO$_2$ catalysts with different SnO$_2$ shell thickness. Reproduced with permission from [66]. Copyright 2017, American Chemical Society (color online).

candidate for tandem catalysis. The enhanced local CO concentration was confirmed on porous Cu shells of Ag@Cu core–shell catalysts, which was evidenced by the *in-situ* measurement and finite-element-method simulations (Figure 6c) [110]. A yolk–shell Ag@Cu$_2$O catalyst was elaborated to serve as a nanoreactor for tandem catalysis of eCO$_2$RR, where the CO produced at the Ag core fluxed to the Cu shell for further reduction (Figure 6d) [93]. Apart from bimetallic catalysts, some monometallic catalysts with core–shell structures are also reported for enhanced eCO$_2$RR performance, such as Cu@Cu$_2$O [111], Cu–Cu$_3$N [112], and Cu–Cu$_2$S [113], which also demonstrate the desirable core–shell structure for eCO$_2$RR. In summary, the fabrication of bimetallic catalysts with core–shell structures has been widely investigated for eCO$_2$RR. By placing the high-activity noble-metal shell on the conductive core, the high selectivity and ultrahigh mass activity can be achieved. More importantly, the favorable electronic and tandem effects endowed by the core–shell structure are highly desirable for eCO$_2$RR.

3.2   Alloys and intermetallics

Given the high flexibility in tuning various properties of catalysts, bimetallic alloys and intermetallics have been

drawing enormous attention in eCO₂RR. Generally, the component, atomic ratio, mixing pattern, particle size, and morphology of bimetallic alloys have a great impact on their eCO₂RR performance. Cu-based alloys account for the most studied alloy catalysts for eCO₂RR [2,114]. A broad range of metals have been reported to alloy with Cu, including both transition metals and main group metals. Cu is able to alloy with metals in a large miscible range, such as Au, Pd, Ni, Al, and Zn. Tan and co-workers [115] reported a supported Cu–Ni alloy nanoparticles with tunable content and uniform distribution, among which the Cu–Ni alloy catalyst with Cu/Ni ratio close to 1 showed the best CO activity and selectivity. Due to the miscibility of Cu and Au, uniform elemental distribution in both bulk and surface region could be obtained on Au–Cu bimetallic nanoparticles, thus a strong composition dependency of eCO₂RR activity and selectivity was often reported over Cu–Au alloys (Figure 7a, b) [47,54]. Similarly, such dependency of eCO₂RR activity on the composition of bimetallic alloys was also reported on Cu–Zn alloy catalyst [57]. On the other hand, Mistry and co-workers [116] reported the eCO₂RR performance on Au–Cu alloy nanoparticles with close composition but different particle sizes from 1.4 nm to 24 nm. With the help of DFT calculation and active machine learning, the Cu–Al alloy was screened for eCO₂RR, enabling favorable C–C dimerization and C₂H₄ pathway [117]. In these alloy catalysts, the atomic arrangement is usually homogenous and random. The atomic mixing pattern of bimetallic catalyst was suggested to play a key role in the activity and selectivity of eCO₂RR. The CuPd nanoalloy with order intermetallic structure exhibited predominant CO production in eCO₂RR, while the one featuring

the phase-separated structure favored C₂ products (Figure 7c) [70]. The order intermetallics with well-defined structure and surface atomic arrangement are attractive catalysts in catalysis [118]. Kim and co-workers [119] reported the effect of atomic ordering of AuCu nanoparticles on eCO₂RR performance. It was found that disorder AuCu alloy catalysts mainly produced H₂, while the CO FE increased with the ordering degree of AuCu alloy catalysts. The highest CO FE was achieved on order intermetallic AuCu nanoparticles with order intermetallic core and three layers of Au metal (Figure 7d). For the thermodynamically immiscible combination of Cu and Ag, it has been revealed that surface alloy with diluted Ag on Cu-enriched surface could be obtained through the galvanic replacement [48,63], and dynamic atomic interdiffusion [64]. The incorporation of Ag in Cu induces strains on Cu–Ag bimetallic surfaces, which is proposed to be responsible for the enhanced formation of CH₄ or C₂₊ oxygenates in eCO₂RR [63,64]. Recently, the author has reported Sn surface-enriched Cu–Sn bimetallic catalysts synthesized by the galvanic replacement, in which Sn tended to incorporate into Cu lattice at low Sn content [120]. The incorporation of Sn sites altered the surface oxophilicity of CuSn bimetallic catalysts, affecting the C₂ pathways through the binding of C₂ intermediates. Cu can also form intermetallic compounds with some metals like Zn, Sn, and In. These intermetallic compounds have also been studied for eCO₂RR due to the well-defined atomic arrangement and great catalytic performance. However, due to the specific stoichiometry, the reported intermetallic catalysts for eCO₂RR are often the mixture of solid solution and order intermetallic compounds, such as Cu–Sn and Cu–In bimetallic
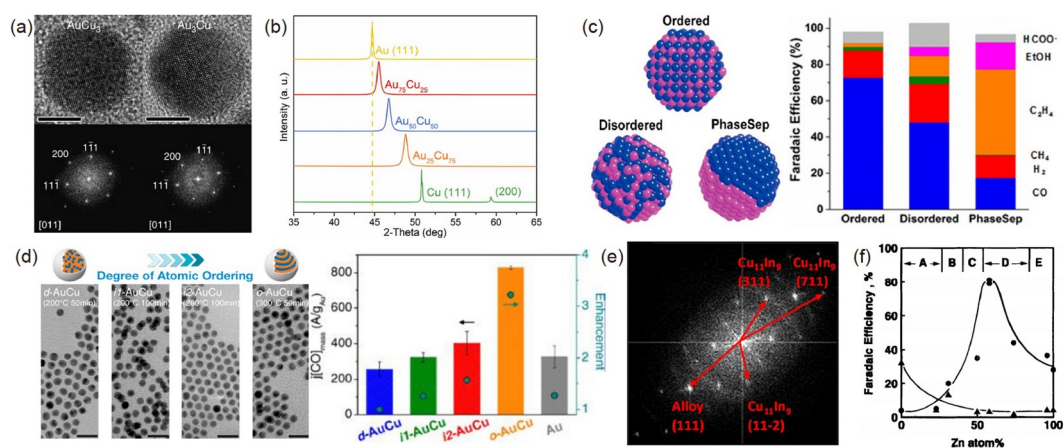

Figure 7 Alloys and intermetallics for eCO₂RR. (a) High-resolution transmission electron microscopy (TEM) image of AuCu₃ and Au₃Cu and fast fourier transform. Reproduced with permission from [47]. Copyright 2014, Springer Nature. (b) XRD patterns of the AuCu bimetallic films with different ratios. Reproduced with permission from [54]. Copyright 2019, American Chemical Society. (c) CuPd bimetallic alloys with different structures and their selectivities in eCO₂RR. Reproduced with permission from [70]. Copyright 2017, American Chemical Society. (d) Atomic ordering transformation of AuCu bimetallic nanoparticles (left) and CO mass activities of AuCu catalysts with different atomic ordering (right). Reproduced with permission from [119]. Copyright 2017, American Chemical Society. (e) The fast Fourier transform image showing the crystallographic reflections of Cu₁₁In₉ intermetallic. Reproduced with permission from [121]. Copyright 2017, American Chemical Society. (f) Effect of Cu–Zn composition and phase on CO FE. Region A: CuZn solid solution+Cu₆₁Zn₃₉; Region B: CuZn solid solution; Region C: Cu₅Zn₈; Region D: Cu₅Zn₈+CuZn₂; Region E: CuZn₂+Zn. Reproduced with permission from [122]. Copyright 1994 Elsevier (color online).

catalysts (Figure 7e) [62,121]. In 1994, Katoh and co-workers [122] have investigated the crystalline phases of Cu–Sn and Cu–Zn alloys and found that the bulk phases of mixed solid solution and intermetallic compounds for Cu–Sn and Cu–Zn have a significant influence on their eCO$_2$RR selectivity. It was proposed that the crystalline intermetallic compounds of Cu$_{5.6}$Sn and Cu$_5$Zn$_8$ were active toward CO$_2$-to-CO conversion and the selectivity was highly dependent on the phases of intermetallics (Figure 7f). For alloy and intermetallic catalysts, electronic and geometric effects are often the main factors affecting their eCO$_2$RR performance due to the specific atomic distribution. Therefore, surface composition and atomic arrangement are often the prior considerations for alloy and intermetallic bimetallic catalysts.

3.3   Hetero-interfaces

Bimetallic catalysts with hetero-interfaces have been extensively studied for eCO$_2$RR and the importance of interface effect is well-documented by both theoretical and experimental results [123]. It should be noted that there are hetero-interfaces in bimetallic catalysts with the core–shell structure, in which the cores usually influence the adsorption and reaction indirectly through the shell. Therefore, here we address the bimetallic catalysts containing interfaces to which both phases contribute in eCO$_2$RR.

As discussed in Section 2.2, the geometric effect in bimetallic catalysts requires more than one binding site and becomes easy to function at the interfaces. Theoretical study has revealed that Au–Cu interfaces were superior to homogenous Au–Cu alloys or monometals in CO$_2$-to-CO performance. The Au–Cu interfaces was proposed to serve as a bifunctional site that stabilized *COOH intermediate by oxygen-affinitive Cu atoms (Figure 8a) [124]. By engineering the interfaces between Cu and In, a more oxophilic metal, high eCO$_2$RR activity and selectivity toward CO were achieved on Cu–In bimetallic catalysts with metallic In supported on Cu surface. The lack of changes in electronic structure and the abundant Cu–In interfaces emphasized the important role of geometric effect at interfaces for stabilizing *COOH intermediate. DFT calculation also supported the hypothesis that the Cu–In interfacial sites outperformed Cu–In alloys for stabilizing *COOH and improving CO selectivity in eCO$_2$RR [73]. The abundant interfaces in Bi–Sn bimetallic catalysts showed the lowest free energy for the formation of *COOH and facilitated the production of formate (Figure 8b) [125]. Similarly, the interface at Cu$_3$Sn/Cu$_6$Sn$_5$ intermetallic heterostructure was proposed to be responsible for the stabilized HCOO* intermediate and formate production [126]. The importance of interfaces was also stressed by Ag–Cu bimetallic catalysts with different biphasic boundaries. The phase-blended Ag–Cu$_2$O possessed

more interphase boundaries than the phase-separated one, which was believed to be the main reason for the enhanced C$_2$H$_5$OH selectivity through a CO-insertion mechanism [88]. Huang and co-workers [104] reported Ag–Cu nanodimers with adjustable interface area and discovered an interface-dependent C$_2$H$_4$ FE. The favorable tandem catalysis and electron transfer through the interfaces accounted for the highest C$_2$H$_4$ selectivity on the Ag$_1$–Cu$_{1.1}$ nanodimer (Figure 8c). The electronic effect induced by the electron transfer through the interfaces in the heterostructured Bi–Cu$_2$S catalyst was also reported to stabilize *OCHO intermediate and boost formate production [127].

Apart from metal–metal interfaces, the metal–metal oxide interfaces also play an important role in improving eCO$_2$RR performance. Jeon and co-workers [57] stressed that maintaining the Cu–ZnO interfaces was critical for the stable CH$_4$ selectivity in eCO$_2$RR. During eCO$_2$RR electrocatalysis, the Cu–ZnO nanoparticles gradually evolved to CuZn alloy due to the reduction of cationic Zn species, leading to the selectivity shift from CH$_4$ to CO. Wang and co-workers [128] attributed the high eCO$_2$RR performance toward two-electron (2e)-transfer products to the abundant Cu/Sn interfaces evolved under reaction condition. Cerium oxides (CeO$_x$) that are inactive for eCO$_2$RR have been widely studied to couple with eCO$_2$RR-active metals, such as Au, Bi, and Cu, for improved catalytic performance. The dissociation of H$_2$O formed OH groups at interfacial Ce^{3+} sites, which helped the stabilization of CO$_2^{\delta-}$ species and subsequent *COOH intermediates [129]. Compared with Bi$_2$O$_3$, the interface in Bi$_2$O$_3$/CeO$_x$ heterostructure was found to benefit the electron transfer and significantly lower the energy barrier for the formate production (Figure 8d) [130]. Moreover, the CeO$_x$ are often used to enhance the formation of C$_{2+}$ products on Cu-based catalysts through the interface effect. The water activation at CeO$_2$ facilitated the formation of *CHO intermediate, which was proposed to be critical for C–C coupling in eCO$_2$RR [131]. The strong interaction between CuO and CeO$_2$ was also reported to promote the stabilization of Cu$^+$ species at metal–metal oxide interfaces under eCO$_2$RR condition, which was proposed to boost C$_2$H$_4$ and suppress H$_2$ production [132]. Zhao and co-workers [133] coated CeO$_2$ nanoparticles on Cu foil and constructed surface-oxidative CuO$_x$ layers that contacted intimately with CeO$_2$, creating favorable Cu–CeO$_2$ interfaces for enhanced C$_{2+}$ production. Except for CeO$_x$, constructing Cu–metal oxide interfaces has been drawing increasingly attention for enhancing C$_{2+}$ production in eCO$_2$RR. For instance, the coating of ultrathin Al$_2$O$_3$ or Al$_2$CuO$_4$ nanosheets supported Cu nanocrystals created abundant heterointerfaces and tailored the orientation, strength, or coverage of *CO intermediate, which favored the energetics of C–C coupling and boosted C$_{2+}$ production (Figure 8e) [134,135]. Wu's group [136,137] reported the utilization of ZrO$_2$ for the modification of Cu
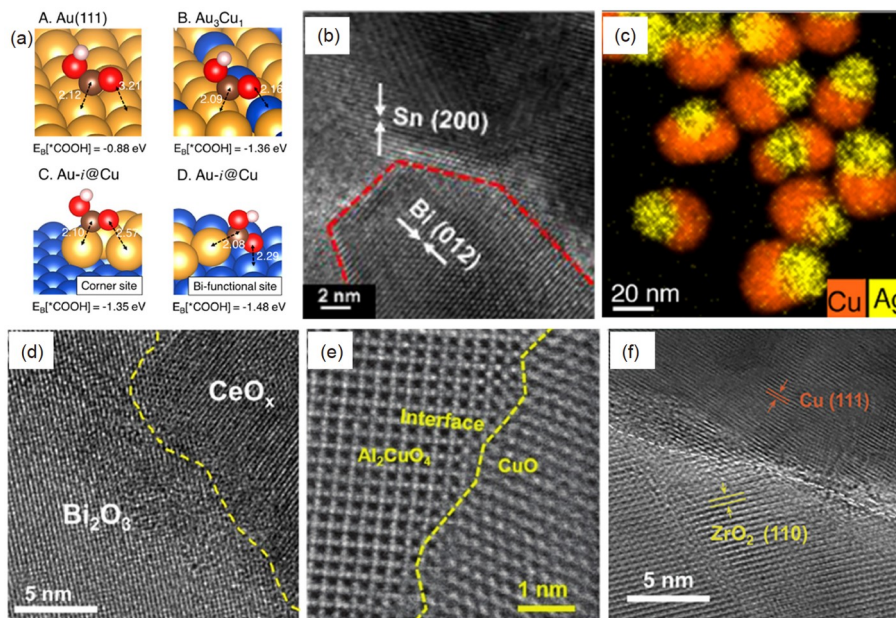
Figure 8 Hetero-interfaces in bimetallic catalysts. (a) Binding configurations of *COOH on Au (111) (A), Au_3Cu_1 (111) (B), and corner site and bifunctional site of Au-*i*@Cu (C, D). Reproduced with permission from [124]. Copyright 2016, American Chemical Society. (b) High-resolution (HR) TEM image of Bi–Sn bimetallic catalysts. Reproduced with permission from [125]. Copyright 2021, John Wiley & Sons, Inc. (c) EDX elemental mapping of Ag_1–$Cu_{1.1}$ nanodimers. Reproduced with permission from [104]. Copyright 2019, American Chemical Society. (d) HR-TEM image showing the interface of Bi_2O_3 and CeO_x. Reproduced with permission from [130]. Copyright 2022, the Royal Society of Chemistry. (e) Atomic resolution scanning transmission electron microscopy (STEM) image of the CuO/Al_2CuO_4 interface. Reproduced with permission from [135]. Copyright 2022, The Royal Society of Chemistry. (f) HR-TEM images of Cu–ZrO_2 interfaces after the eCO_2RR test. Reproduced with permission from [137]. Copyright 2022 Elsevier (color online).

electrodes and achieved high C_{2+} selectivity (Figure 8f). The interfacial boundaries between Cu and crystalline or amorphous ZrO_2 were suggested to serve as a dual-site catalyst that was able to activate CO_2 and stabilize *CO.

3.4 Single atom alloy

Single atom alloy (SAA) is a kind of unique alloy system, where low-content metal component disperses in another metal matrix in the form of single atoms. This special alloying mode results in a significant change in the electronic structure by incorporating isolated solute atoms, thus leading to the drastic change in the adsorption behavior and catalytic performance [138,139]. In AgCu single atom alloy, the diluted Cu atoms are isolated and surrounded by Ag atoms, showing ultra-narrow d band and free-atom-like electronic property of Cu. The unique Cu 3d state in AgCu SAA gave rise to strong binding strength to adsorbates and thus exhibited enhanced catalytic kinetics compared with bulk Cu [140]. Theoretical study has demonstrated that Cu-based SAA catalysts with diluted Co single atoms were promising candidate for CH_3OH production in eCO_2RR due to the narrowed d-band of solute Co atoms [141]. DFT study also suggested that Au- or Ag-based SAA catalysts with isolated Rh atoms could serve as a tandem catalyst to effectively convert CO produced at Au or Ag into CH_4 in eCO_2RR [142]. The PbCu SAA catalyst with Pb single atoms in the

Cu matrix lost the selectivity of Cu catalysts and exhibited excellent CO_2-to-formate activity in eCO_2RR due to the altered adsorption configuration and reaction pathway [143,144]. Similarly, the $Cu_{97}Sn_3$ SAA catalyst with trace amount of isolated Sn atoms also significantly change the selectivity of Cu-based catalysts in eCO_2RR, showing high CO FEs that are even comparable to noble metals (Figure 9) [144–146]. These results demonstrate that SAAs catalysts are promising candidates for achieving high activity and selectivity in eCO_2RR. Precisely designed SAA catalysts also provide an ideal model catalyst to study the effects of electronic, geometric and tandem effects on the eCO_2RR performance of bimetallic catalysts. Therefore, more SAA catalysts should be developed for eCO_2RR and more attention should be paid to identify the respective role and synergy of solute and solvent atoms in SAA catalysts for the improved eCO_2RR performance.

3.5 *Operando* reconstruction

It should be noted that the stability and reconstruction of bimetallic catalysts under eCO_2RR conditions must be carefully considered as the combination of different metals is likely to bring about metastability and complexity in bimetallic catalysts [34]. The structural stability and the understanding of the dynamic structural reconstruction of the bimetallic catalysts during eCO_2RR electrocatalysis are im-
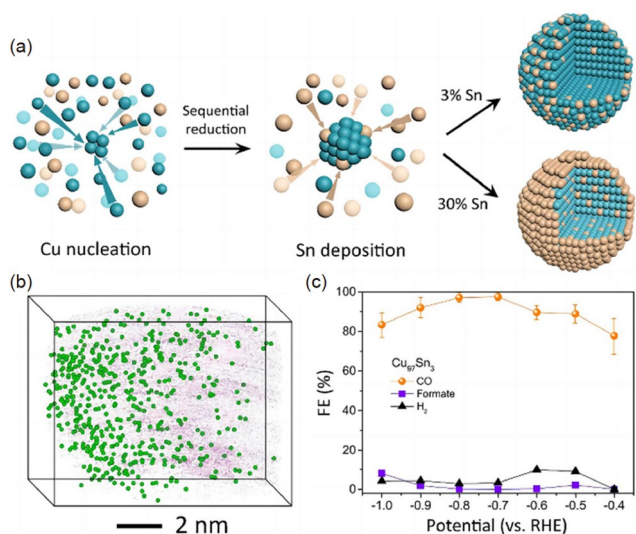
Figure 9   (a) Schematic illustration of the Cu₉₇Sn₃ SAA and Cu₇₀Sn₃₀ nanoparticle formation *via* the sequential reduction. (b) 3D tomography of the $Cu_{97}Sn_3$ SAA nanoparticle demonstrates the distribution of Sn atoms (green) in the Cu matrix (purple). (c) The potential-dependent FEs of $Cu_{97}Sn_3$ SAA. Reproduced with permission from [146]. Copyright 2021 Springer Nature (color online).
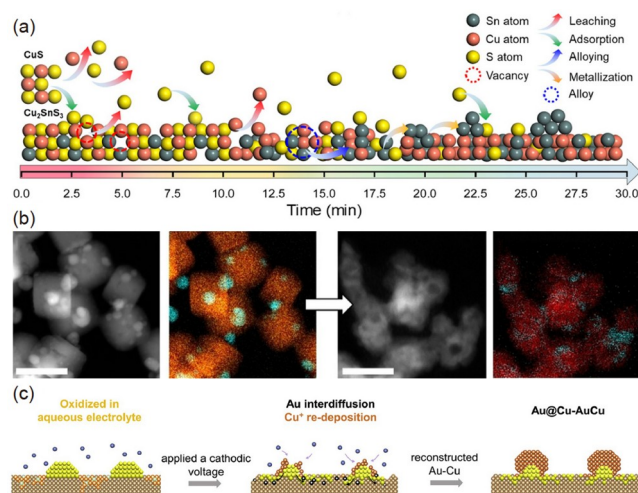

Figure 10   (a) Schematic illustration of the *in-situ* dynamic construction process of the CuSn sulfide catalyst. Reproduced with permission from [147]. Copyright 2022, American Chemical Society. (b) The eCO_2RR reaction-driven redispersion of Ag decorated Cu_2O nanocubes. Reproduced with permission from [150]. Copyright 2021, John Wiley & Sons, Inc. (c) The structural reconstruction of epitaxial Au–Cu heterostructure under eCO_2RR. Reproduced with permission from [94]. Copyright 2022 Elsevier (color online).

portant and desired for the development of efficient electrocatalysts. On one hand, the restructured phases in bimetallic catalysts during the electrocatalysis serve as the real active centers for eCO_2RR. For instance, the hybrid composed of Cu_2SnS_3 and CuS underwent *in-situ* dynamic reconstruction under eCO_2RR condition and evolved into stable Sn-/S-doped $Cu_{24}Sn_{20}$ alloy, which served as the real active phase for eCO_2RR (Figure 10a) [147]. On the other hand, at present, the characterizations of bimetallic catalysts are often focused on the as-prepared nanostructures before the electrocatalysis, which may lead to misunderstandings of the structure–activity relationship by the *ex-situ* investigation [148]. It was found that the surface reconstruction of Cu overlayers on Pt surfaces had to be considered to understand the selectivity behavior. The strong Pt–CO binding was proposed to drive the aggregation of Cu atoms and the exposure of Pt surfaces, leading to the inferior eCO_2RR activity and increasing HER [106]. Similarly, the model catalysts comprising the Cu monolayer and multilayer on the Au(111) surface were suggested to undergo the surface segregation under the operating condition in alkaline, forming the near-surface Cu/Au alloy [60].

In some cases, the restructured catalyst surfaces evolved under reaction conditions are critical for eCO_2RR. The hierarchical Sn–Cu catalysts evolved a core–shell structure comprising *in-situ* reconstructed Sn/SnO_x shells and heterogeneous Sn–Cu alloy/Sn cores. The unique Sn/SnO_x shell formed under eCO_2RR was proposed to be important for stabilizing HCOO* intermediate and suppressing HER, contributing a high FE of C_1 products [149]. The reaction-

induced redispersion of Ag nanoparticles on Cu_2O nanocubes during eCO_2RR gave rise to the interplay of multiple favorable effects that were responsible for the enhanced C_{2+} liquid production (Figure 10b) [150]. Similarly, the Ag-modified Cu nanowire catalyst was found to undergo an irreversible surface restructuring driven by the reoxidation/reduction process under eCO_2RR condition. The atomic interdiffusion between Ag and Cu facilitated the formation of surface CuAg alloy, which was responsible for the enhanced CH_4 through strain and ligand effects [64]. Recently, Zhu and co-workers [94] reported the direct observation of the dynamic restructuring of epitaxial Au–Cu bimetallic heterostructure by tracking and visualizing the structural change and atomic migration in eCO_2RR. The resulting heterostructure contained AuCu alloy and Au@Cu core–shell nanoparticles, enabling increased C_{2+} alcohols production *via* the tandem mechanism (Figure 10c).

4   Advances in bimetallic catalysts for eCO₂RR

4.1   Classification

Metal-based electrocatalysts used in eCO_2RR are often classified by their main reduction products due to their distinctive selectivity behaviors. In 1985, Hori and co-workers [6] systematically studied the electrochemical reduction of CO_2 on different metal electrodes and identified four groups of metals based on their selectivity characteristics. Group I contains metals of Au, Ag, and Zn, producing predominantly CO in eCO_2RR. Metals in Group II are usually main group

metals, such as Sn, Pb, Bi, and In, with the high selectivity toward formate. Apart from these main-group metals, Pd is also known as a unique metal in eCO_2RR due to its ability to reduce CO_2 into either CO or formate, which is largely dependent on the applied potential [151,152]. The Pd-based catalysts exhibited the high selectivity toward formate at low overpotentials, which is favorable for the energy efficiency. Besides, Pd is believed to stabilize *COOH but suffer from strong *CO binding [153]. Therefore, we classify Pd as a formate-producing metal here. Cu is the only metal in Group III, exhibiting unique selectivity toward valuable deep reduction products, including various hydrocarbons and oxygenated compounds. Other common transition metals, such as Fe, Co, Ni, and Pt, mainly showed HER activity rather than CO_2 reduction under eCO_2RR condition. Due to the strong selectivity of monometallic electrocatalysts in eCO_2RR, it is generally to classify the metal-based metals by their main reduction products in eCO_2RR, including CO-producing metals (M_{CO}), formate-producing metals (M_{HCOOH}), Cu, and hydrogen-producing metals (M_H).

The grouping of metals based on the selectivity could be rationalized by the adsorption energies of adsorbates on metal surfaces. For instance, four groups of metal can be distinguished by the binding energies of *COOH, *CO, and *H (Figure 11a). Cu separates itself from other metals and is identified as a potential candidate for products beyond CO, since Cu is the only metal that possesses moderate *CO binding energy but near-zero *H binding energy [154]. Vasileff and co-workers [2] classified the second component of Cu-based bimetallic catalysts by the affinities toward H and O atoms as some key intermediates are either C- and H-containing or O-binding (Figure 11b). The bimetallic surfaces provide multiple sites with different affinity toward O and H and thus change the binding strength of different intermediates. Based on these binding and affinity characteristics, the distinct selectivity of monometallic catalysts is almost predictable in eCO_2RR. However, when two metals are coupled together, the selectivity trends on bimetallic

catalysts are not as predictable as those on monometallic catalysts, which is likely due to the complex electronic properties and geometric coordination on the surface of bimetallic catalysts. For example, enhanced selectivity toward various products has been reported on Cu–Ag bimetallic catalysts, including CO, C_2H_4, and C_2H_5OH [79,155,156]. Therefore, in the following, we will discuss the advances of bimetallic catalysts based on their selectivity in eCO_2RR and try to elucidate some rules of selectivity trends for bimetallic catalysts.

4.2 CO_2 to CO and formate

CO and formate are both two-electron-transfer products, the simplest eCO_2RR reduction products. Not only do they have a lot in common in their paths, but they also have a lot in common in their bimetallic combinations. For example, combinations of Cu and formic acid product metals often exhibit adjustable selectivity between CO and formate [128,157,158].

CO and formate are both promising 2e products in CO_2RR. The former is a gas-phase product and the latter is a liquid-phase product. Therefore, it is desirable that they can be obtained with the high and tunable selectivity on Cu–M_{HCOOH} bimetallic catalysts as no additional separation process is needed. It has been shown that the composition of Cu–M_{HCOOH} bimetallic catalysts has a great influence on the selectivity between CO and formate. Hoffman and co-workers [121] demonstrated that the mixed phases of dendritic Cu–In alloys varied with the In content. Due to the altered adsorption strength of intermediates, the products that consisted of formate and syngas exhibited a composition-dependent selectivity. The composition-dependent selectivity trend has been also observed on electrodeposited Cu–Sn alloys, among which $Cu_{87}Sn_{13}$ showed an enhanced CO selectivity and $Cu_{55}Sn_{45}$ exhibited high formate selectivity. Furthermore, in all Cu–Sn alloys, the high HER activity on Cu was inhibited by Sn introduction [62]. Similarly, Huo and co-workers [159] found that a small portion SnO_x (6.2%) in CNT-supported Cu/SnO_x heterostructures gave a remarkable selectivity shift toward CO with the maximum FE of 89%, while the formic acid became the main product on the SnO_x-enriched sample.

4.2.1 CO

Bimetallic catalysts with CO as the main reduction product often contain at least one of M_{CO} metals. It is reasonable to expect that CO remains the main reduction product on bimetallic catalysts consisting of two M_{CO} metals. Although these metals come from the same group, the favorable effects of bimetallic catalysts are still suitable for these bimetallic combinations in terms of the enhanced CO activity and selectivity, such as Au–Ag alloy- and Ag nanoparticles-deco-

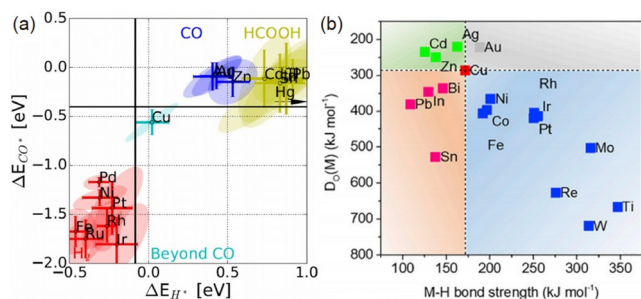
Figure 11 Metal classification. (a) The metal classification by the ΔE_{CO*} and the ΔE_{H*} as descriptors. Reproduced with permission from [154]. Copyright 2017, John Wiley & Sons, Inc. (b) The intermediate M–H bond strength plotted as a function of the bond dissociation enthalpy of metal oxides. Reproduced with permission from [2]. Copyright 2018 Elsevier (color online).

rated ultrathin Zn nanoplates [160,161]. Recently, Zhang and co-workers [162] reported a Zn–Ag–O catalyst with "ship-in-bottle" structure. The electronic structure of the catalyst was regulated by abundant Zn–Ag–O heterointerfaces, which lowered the energy barrier for HCOO* formation and realized a high energy efficiency of CO_2-to-CO conversion (Figure 12a).

The enhanced CO production in eCO_2RR has also been frequently reported on M_{CO}–Cu bimetallic catalysts. On one hand, the usage of the noble metals (Au and Ag) can be minimized by coupling with the less expensive Cu metal, thus leading to increased CO mass activity [119]. Choi and co-workers [163] prepared Ag–Cu dendrite catalysts by the electrodeposition and improved the cost-effectiveness of the catalysts in terms of Ag mass activity. Similarly, Lee and co-workers [164] modified Cu foam with Ag or Au by galvanic replacement reaction. Ag mainly existed as metallic Ag on the surface, while Au formed Au–Cu alloy. Thanks to the foam-like structure and the decreased use of Ag and Au, the Ag/Cu and Au/Cu foam catalysts showed greater cost-effectiveness than Ag and Au films. Zhou and co-workers [35] demonstrated that the thin-walled hollow Au–Cu nanoparticle is also an efficient structure for increasing the Au mass current density. However, the hollow Au–Cu nanoparticles lost their eCO_2RR activity after thermal annealing due to the segregation of Cu to the surface and the reduced surface defects. On the other hand, the catalytic performance

of eCO_2RR, such as the overpotential [165], CO selectivity [166], and CO production rate [167], can be enhanced on Cu–M_{CO} bimetallic catalysts. Chen and co-workers [168] demonstrated that the Au-coated Cu nanowire array with a high surface area enhanced the overall current density for the syngas product. Kottakkat and co-workers [155] reported that, compared with Ag foam, the overpotential of CO production could be reduced by 187 mV on electrodeposited AgCu foam. Syngas is also attractive product from eCO_2RR, as the syngas with different CO/H_2 ratios can be converted into valuable chemicals through existing industrial technologies. Ross and co-workers [49] revealed that the surface electronic structure could be tuned by the surface ratio of Au and Cu atoms. The binding strength of *CO and *H could be systematically modulated by the surface Cu coverage. As a result, syngas production with suitable CO/H_2 ratio and high reaction rate was realized. Similarly, Lamaison and co-workers [169] prepared a series of dendritic Zn–Cu foam electrodes with different amounts of Cu by the electrodeposition method. Within the suitable Cu content range, the CO/H_2 ratio of syngas seemed to be related closely with the composition of Zn–Cu but independent of the applied potential. Consequently, controllable CO/H_2 ratio and high current density were achieved simultaneously.

The weakened *CO binding strength and the diluted Cu sites on Cu–M_{CO} bimetallic catalysts are mainly responsible for the enhanced CO production. Hirunsit *et al.* [170] re-
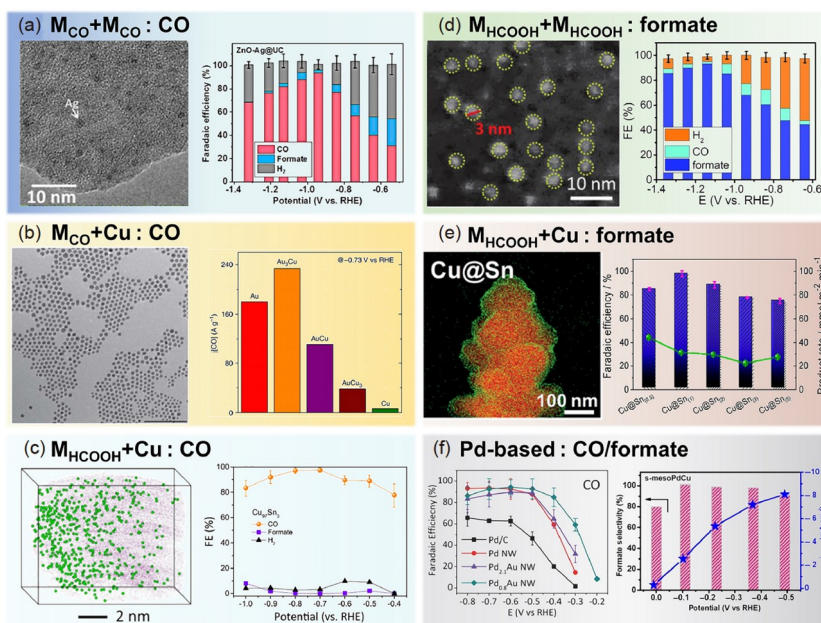
Figure 12   CO and formate products on bimetallic catalysts. (a) TEM image and CO FE on ZnO–Ag bimetallic catalyst. Reproduced with permission from [162]. Copyright 2021, American Chemical Society. (b) TEM image and CO mass activity on AuCu bimetallic catalysts. Reproduced with permission from [47]. Copyright 2014, Springer Nature. (c) 3D tomography and FEs of eCO_2RR of bimetallic $Cu_{97}Sn_3$ nanoparticles. Reproduced with permission from [146]. Copyright 2021, Springer Nature. (d) TEM image and FEs of eCO_2RR on Bi–SnO_2 bimetallic catalyst. Reproduced with permission from [185]. Copyright 2018, John Wiley & Sons, Inc. (e) EDS mapping and formate FE on bimetallic combination of Sn and Cu [197]. (f) 2e products of eCO_2RR on Pd-based bimetallic catalysts. Reproduced with permission from [181]. Copyright 2018, John Wiley & Sons, Inc. Reproduced with permission from [201]. Copyright 2021, Chinese Chemical Society (color online).

ported that the adsorption energy of *CO on Cu_3Au was weakened by 0.19 eV compared with Cu using DFT calculations. Liu and co-workers [54] suggested that the electronic structure of Au–Cu alloy changed with the increased Au content, resulting in the weakened binding energy of *CO intermediate. Generally, with the increasing proportion of M_{CO} metal in Cu–M_{CO} bimetallic catalysts, the CO production increased at the expense of deep reduction products. Christophe and co-workers [171] suggested that the diluted surface Cu sites in Au–Cu alloy prevented the formation of hydrocarbons and the presence of Au sites promoted the CO desorption. CO production increased while the CH_4 product diminished with the increased Au content. Similarly, Kim and co-workers [47] observed that the number of products and the corresponding FEs decreased with the increasing Au content in Au–Cu bimetallic nanoparticles. The composition of Au–Cu bimetallic nanoparticles could tune the binding strength of the intermediates and thus modulate the reduction products. In particular, the Au_3Cu bimetallic nanoparticle exhibited an excellent CO mass activity that outperformed the conventional Au nanoparticles by more than an order of magnitude (Figure 12b). Kim and co-workers [55] demonstrated that the electron transfer from the polycrystalline Cu substrate to the Au thin layer changed the electronic structure of the Au layer, leading to the superior CO activity and selectivity on the thin Au layer on Cu compared with the polycrystalline Cu and Au.

Another important class of bimetallic catalysts that possess high CO selectivity in eCO$_2$RR consisted of Cu and M_{HCOOH} metals, including In, Sn, and Pd, which exhibited comparable or even superior CO FE to noble metals. In 2015, Takanabe *et al.* [172,173] investigated the influence of In incorporation into Cu on the eCO$_2$RR performance. Their studies suggested that the Cu–In alloy exhibited high CO$_2$-to-CO selectivity with suppressed HER on matter the alloy derived from In electrodeposition on OD-Cu or reduced CuInO$_2$. However, other researchers suggested that alloying was not necessary for Cu–In bimetallic catalysts to achieve high CO selectivity in CO$_2$RR. Larrazábal *et al.* [174] reported that the Cu and In gradually segregated to form a core–shell structure with the Cu-enriched core and In(OH)$_3$ shell in In$_2$O$_3$-supported Cu NPs or CuInO$_2$ under the eCO$_2$RR conditions, which was real active species. Instead of forming Cu–In alloys, Luo and co-workers [73] showed that the Cu–In interfaces in the metallic In NPs-decorated Cu nanowires exhibited a high CO FE of ~95% at −0.6 to −0.8 V$_{RHE}$. The interfaces stabilized the *COOH intermediate through geometry effect and suppressed the *H adsorption, which increased the CO selectivity. Recently, Chu and co-workers [99] developed a facile wet chemical method to prepare a Cu and In oxides deposited on nitrogen-doped carbon nanotubes as catalysts for eCO$_2$RR. The metal oxide interfaces that were tuned by the metal ratio showed com-

position-dependent CO selectivity trends. Although the metallic species were believed to act as the active sites in eCO$_2$RR, they proposed that the synergistic effect between CuO and In$_2$O$_3$ in the heterostructure played an important role in the enhanced eCO$_2$RR performance. Except for In, combining Cu with Sn has also exhibited the enhanced CO selectivity in CO$_2$RR [175]. Sarfraz and co-workers [72] electrodeposited Sn on oxide-derived Cu and the alloying of Cu and Sn inhibited the adsorption of *H and the hydrogenation, resulting in high CO FE over 90% at −0.6 V$_{RHE}$. Similarly, Li and co-workers [66] coated Cu NPs with thin controllable SnO$_2$ layers, which exhibited a high CO FE of 93% with a current density of 4.6 mA cm^{-2} at −0.7 V$_{RHE}$. Schreier and co-workers [176] modified CuO NWs with SnO$_2$ by the atomic layer deposition (ALD) method, which guaranteed controllable and uniform coating of SnO$_2$. The enhanced CO selectivity was attributed to the suppressed *H adsorption and the facilitated CO desorption. Apart from the composition, the dendritic morphology of Sn–Cu bimetallic catalysts has been demonstrated to be a favorable structure for CO production in eCO$_2$RR, which improved the mass transport and provided abundant active sites [177,178]. Further, the Cu–Sn bimetallic catalysts incorporated in gas diffusion electrode (GDE) also exhibited high CO selectivity at high current density in a flow-cell electrolyzer, demonstrating the potential for practical application of eCO$_2$RR [179]. Recently, it has been reported that trace amount of Sn incorporated in Cu matrix could tame the selectivity of Cu and produce near-unity CO selectivity in eCO$_2$RR [145]. The atomically doping of Sn in Cu was proposed to be crucial for the excellent CO selectivity [144]. Ren and co-workers [146] synthesized Cu–Sn single-atom surface alloy with only 3% Sn-atomically-decorated Cu surface, achieving a peak CO FE of 98% at −0.7 V$_{RHE}$ (Figure 12c). Similarly, we have recently obtained a high CO FE of 96.36% with a CO current density at −0.8 V$_{RHE}$ on a Cu–Sn catalyst with highly dispersive surface Sn [120]. Due to the excellent CO$_2$-to-CO performance, the SnO$_2$-modified Cu have recently showed promising practical application and delivered a solar-to-chemical energy conversion efficiency up to 19.9% by integrating a photovoltaic cell with a gas diffusion eCO$_2$RR system [180].

It is interesting to note that the combination of M_{CO} and M_{HCOOH} often shows the selectivity toward formate instead of CO, while combining M_{CO} with Pd has been reported to reduce the overpotential and increase the FE for CO (Figure 12f) [181]. Lin and co-workers [153] reported that the overpotential for reaching CO current density of 1 mA cm^{-2} could be reduced from −0.76 V on Ag NPs to −0.55 V on PdAg NPs. The strong adsorption of CO on Pd was proposed to increase the coverage of *CO on the Au–Pd alloy film, which promoted CO production at low overpotential and suppressed the competing HER [182]. As a bifunctional

metal, Pd exhibits switchable FEs toward CO or formate in eCO$_2$RR. The bimetallic combinations of Cu and Pd have been reported to promote the selectivity to either CO or formate [183]. Mun and co-workers [184] reported a monodisperse Cu–Pd NPs with CO FE of 87%, in which Pd was found to block the protonation of *CO for the further reduction on the Cu–Pd surface. On the other hand, Li and co-workers [36] suggested that Pd served as the binding sites and active centers for CO production in eCO$_2$RR, while Cu atoms contributed to the stabilization of *COOH and the desorption of *CO on Pd through electronic interaction.

4.2.2   Formate

Similar to CO-producing bimetallic catalysts, M$_{HCOOH}$ metals usually participate in constituting bimetallic catalysts with formate as the main reduction products. The bimetallic combination within M$_{HCOOH}$ groups is a promising way to achieve high formate FE at reduced overpotentials. The Bi nanoparticles-decorated Sn nanosheets provided abundant favorable sites at the interfaces, which delivered a high formate FE of 96% with the excellent stability up to 100 h (Figure 12d) [185]. The favorable Bi–Sn interfaces and interconnected 3D channels in the Bi–Sn aerogel jointly contributed to the high formate selectivity in a wide potential range [125]. The strategies for the scaled synthesis of Bi–Sn bimetallic catalysts have been developed, which exhibited a promising formate activity for practical application, such as Bi-decorated amorphous SnO$_x$ nanosheets and eutectic Bi–Sn nano-alloys [186,187]. Other M$_{HCOOH}$ bimetallic catalysts have also been investigated in eCO$_2$RR, such as In–Sn and Sn–Pb alloys [188–191], which outperform any monometallic counterpart with regard to CO$_2$-to-formate activity and selectivity.

The M$_{HCOOH}$ metals exhibits strong selectivity genes that can be passed to the corresponding bimetallic catalysts. For instance, eight Sn–M bimetallic catalysts derived from metal stannate were tested for eCO$_2$RR and 5 of them produced formate as main reduction products, among which Cu–Sn and Ag–Sn were the best [192]. Cu–M$_{HCOOH}$ is a common bimetallic combination that exhibited high formate activity in eCO$_2$RR. The formate-producing metals are mainly p-block elements, including Sn, In, Pb, and Bi. Compared with Cu, they are usually more oxyphilic and exhibit inhibited HER. Consequently, coupling Cu with M$_{HCOOH}$ is an efficient way to tune the binding strength of intermediates and suppress the HER activity of Cu [121]. Different from diverse product distributions on Cu–M$_{CO}$ bimetallic catalysts, the selectivity trends of Cu–M$_{HCOOH}$ bimetallic systems are relatively simple. Early studies have shown that the main products obtained on Cu–M$_{HCOOH}$ bimetallic catalysts are CO and formate [31,122]. Jia and co-workers [193] prepared Cu–Bi bimetallic catalysts by the *in-situ* reduction of CuBi$_2$O$_4$ microspheres. The synergistic effect between Cu

and Bi in reduced Cu–Bi bimetallic catalyst gave a maximum formate FE of ~95% at −0.93 V$_{RHE}$. Zu and co-workers [194] demonstrated that the introduction of Cu into Bi nanocrystals modified the electronic structure of Bi and changed the HCOOH formation pathway from *COOH intermediate to OCHO* intermediate, leading to a high formate FE over 80% in a wide potential range. Electrodeposition method was frequently utilized to prepare Cu–M$_{HCOOH}$ bimetallic catalysts on conductive substrate. Ye and co-workers [195] electrodeposited Sn on Cu substrate, forming Sn–Cu alloy on Cu foam. The HER was suppressed on the surface of Sn–Cu alloy and the stepped (211) surface of Sn–Cu alloy was proposed to be selective for HCOOH. Peng and co-workers [196] electrodeposited Cu–Sn alloy on N-doped carbon cloth, on which the N doping provided the sites for the nucleation and growth of Cu–Sn alloy. The porous structure and abundant active sites contributed a high formate FE of 90.24% with a large partial current density of 15.56 mA cm^{-2} at −0.97 V$_{RHE}$. Hou and co-workers [197] prepared a 3D porous Cu@Sn electrode with a core–shell structure by two-step electrodeposition. The dendritic structure of Cu as well as the deposited Sn grains was highlighted, which enlarged the specific surface area and boosted the mass activity (Figure 12e). Wang and co-workers [126] electrodeposited Sn on foam Cu substrates and an intermetallic CuSn heterostructure consisting of Cu$_3$Sn/Cu$_6$Sn$_5$ formed by subsequent annealing. The heterostructures exhibited a high selectivity of HCOOH in the both H cell and flow cell, which was attributed to the favorable HCOO* intermediate formation and moderate adsorption of *H. Similarly, dendritic Cu–Bi bimetallic catalysts on Cu substrates were also obtained by the electrodeposition, where the intimate contact between Cu and Bi grains contributed to abundant defects as active sites and tuned the binding strength of the intermediates [198]. Pd is known for achieving formate at low overpotential, while Pd suffers from the deactivation in eCO$_2$RR due to CO poisoning. Therefore, Pd is often modified by the second component to further improve formate selectivity and catalytic stability. For example, the Pb–Pd bimetallic catalyst showed the better formate FE than pure Pb and better stability than pure Pd [199]. Carbon-supported Pd–Sn alloy catalyst was reported to produced exclusively formate from eCO$_2$RR on at a low overpotential of −0.26 V [200]. Similarly, Lv and co-workers [201] obtained high formate FE close to 100% at only −0.1 to −0.4 V$_{RHE}$ on single crystalline mesoporous Pd–Cu bimetallic catalysts, which also exhibited an outstanding stability with almost no deactivation during 15,000 s of eCO$_2$RR (Figure 12f).

Compared with Cu, combining Cu with M$_{HCOOH}$ often exhibits enhanced CO or/and formate selectivity with suppressed HER. The M$_{HCOOH}$, such as Sn, Bi, and In, is known as the poor activities for HER [202]. Generally, Cu combined with a small portion of M$_{HCOOH}$ exhibited high CO se-

lectivity, while the selectivity shifted to formate when M_{HCOOH} was dominated in the Cu–M_{HCOOH} bimetallic catalysts [62,121,159]. In addition to the composition, the different structures of the Cu–M_{HCOOH} bimetallic catalysts are proposed to play a key role in the enhanced CO or formate selectivity. Alloys or surface alloys [72,172,173,195], intermetallic heterostructures [126], interfaces between metals, oxides, or hydroxides [73,128,174,203], have been proposed to determine the formation of the decisive intermediates. However, the key properties of Cu–M_{HCOOH} catalysts that influence the selectivity between CO and formate are still unclear. As the simplest reduction products in eCO$_2$RR, two electrons are needed to be transferred to CO$_2$ for the formation of CO and formate. Through the first proton-/electron-pair transfer to CO$_2$, two important intermediates can be formed, namely, the *COOH intermediate with C atoms bonded to the surface and the *OCHO intermediate with O atom bonded to the surface. For the 2e products, both CO and formate can be produced through the *COOH intermediate, while only formate can form *via* the *OCHO intermediate [194]. Based on the DFT study, restrict scaling relationship existed between the adsorbed *H and *COOH on different metals surfaces [204]. Therefore, it is unlikely that high formate selectivity could be achieved if *COOH was the key intermediates for formate product. Furthermore, it was found that the binding energies of *COOH and *OCHO served well as the descriptors for CO and formate production, respectively [13]. Therefore, the selectivity trends are often interpreted through the binding strength of the relevant intermediates, including *OCHO, *COOH, and *CO, on Cu–M_{HCOOH} bimetallic catalysts as they mainly produce CO and formate in eCO$_2$RR [121,128]. The facilitated formation of *COOH and desorption of *CO often contributed to the high CO selectivity obtained on Cu–M_{HCOOH} bimetallic catalysts, such as CuO–In$_2$O$_3$ [99], In islands on Cu[73], Cu/ SnO$_2$ core–shell NPs[66]. On the other hand, the promoted *OCHO pathway is often considered for the catalysts that showed enhanced formate production [195]. For instance, the Cu doping was supposed to modulate the electronic environment of Bi nanocrystals and alter the pathway from *COOH to *OCHO intermediate [194]. The formation of *OCHO intermediate was suggested to be the limiting step on Cu–Sn alloys, while *COOH was the relevant intermediate for CO and formate formation of Cu and Sn [205].

4.3 CO$_2$ to deep reduction products

In eCO$_2$RR, deep reduction products need more than two-electron-transfer steps and are usually valuable chemicals, mainly including CH$_4$, CH$_3$OH, C$_2$H$_4$, C$_2$H$_5$OH, and *n*-C$_3$H$_7$OH. Cu is the only metal that is capable of reducing CO$_2$ into deep reduction products, while at the same time suffers from the high overpotential, dissatisfactory selectiv-

ity, and unwanted HER competition. Bimetal strategy has been proved to be an effective way to improve the eCO$_2$RR performance of Cu-based catalysts, especially the selectivity.

The improvement in total C$_{2+}$ products is highly desired and is often realized on Cu-based bimetallic catalysts. Given the low HER activity and the importance of *CO intermediate for the further reduction, CO-producing metals are often the favorable choices as the second component to combine with Cu. The Au nanoparticles-decorated Cu$_2$O nanowire-derived Cu–Au bimetallic catalyst exhibited a total C$_{2+}$ FE of ~70%, which was nearly 30% higher than Cu$_2$O nanowire catalyst [78]. Unlike Au, which can form homogeneous alloy with Cu, Ag is immiscible with Cu at room temperature [63]. Thus, Ag–Cu bimetallic combination is promising candidate for C$_{2+}$ production through electronic, geometric and tandem effects. The core–shell-structured Cu–Ag bimetallic catalysts are often designed for eCO$_2$RR. The thickness of outer Ag shells was found to be critical to achieve higher C$_{2+}$ FE than bare Cu counterpart (Figure 13a) [108,206], as the increasing Ag shell may intensify the production of CO. Recently, the porous Cu shell over Ag nanosphere core was designed and the Cu shell with an optimal average pore diameter of 4.9 nm showed the highest C$_{2+}$ FE up to 73.7% through the enhanced local *CO coverage [110]. Although Ag and Cu are immiscible in bulk at room temperature, it has been demonstrated by EXAFS that Ag–Cu bonds existed in electrodeposited Cu–Ag wires with only 6% Ag, suggesting the partially alloying of Ag and Cu. The homogeneously mixed Cu–Ag was proposed to be critical for the high C$_2$ FE (C$_2$H$_4$ and C$_2$H$_5$OH) up to ~85% at −0.7 V$_{RHE}$ in a flow electrolyzer [207]. Apart from M$_{CO}$ metals, other metals, such as Pb and Ni [109,208], are also reported to alloy with Cu for enhanced C$_{2+}$ production. The C$_{2+}$ FE increased from 42.4% on pure Cu NPs to 73.5% on Cu–Pb NPs with an ultrathin Pb shell of 0.7 nm (Figure 13b) [109]. Recent studies on Cu–Pd bimetallic catalysts showed excellent C$_{2+}$ FE up to 89% with a large current density of 500 mA cm^{-2} in acidic media, demonstrating tremendous potential for the application [209]. The C$_{2+}$ production can also be promoted significantly by heterointerfaces between Cu and metal oxides. CeO$_2$ nanoparticles-coated Cu foil created abundant Cu–CeO$_2$ interfaces and drastically increased C$_{2+}$ FE to 61%, while the undecorated Cu foil showed only 23% of C$_{2+}$ FE under the same condition [133]. It was suggested that the interplay between CeO$_2$ and Cu enhanced H$_2$O activation by CeO$_2$ and thus facilitated the formation of *CHO, which was critical for C–C coupling and high C$_{2+}$ FE [131]. The interfacial effect in Cu–ZrO$_2$ catalysts could also stabilize the atop *CO intermediate and lower the energy barrier for C–C coupling, thus exhibiting a high C$_{2+}$ FE up to 85% (Figure 13c) [136,137]. In short, the FE of total C$_{2+}$ products has been significantly improved by the bimetallic strategy. However, it is still difficult but de-
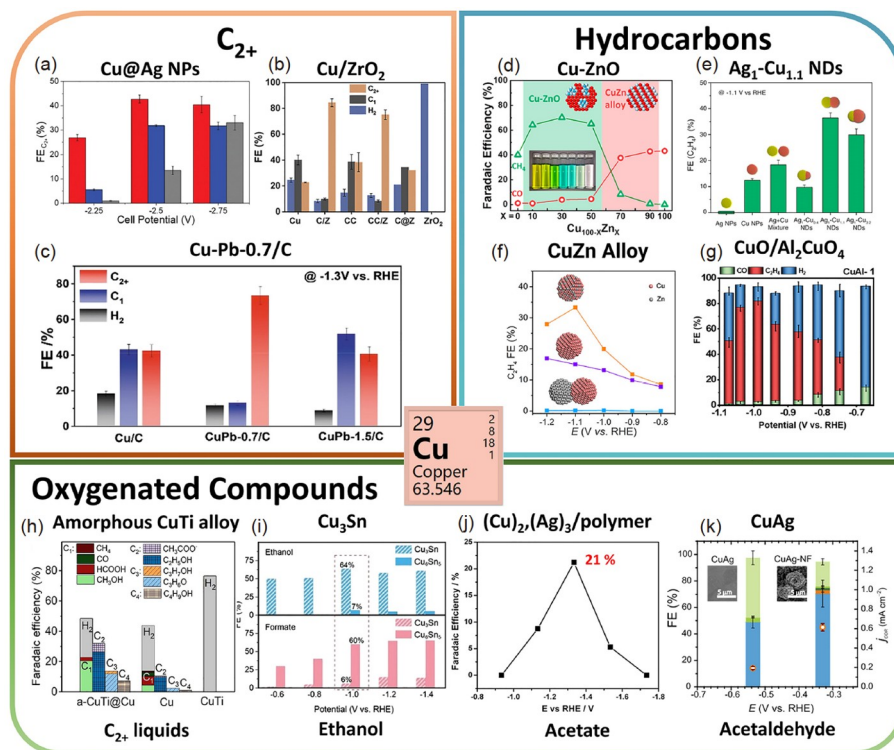
Figure 13 Deep-reduction products on bimetallic catalysts. (a) FE of C_{2+} products on Cu@Ag. Reproduced with permission from [108]. Copyright 2021, John Wiley & Sons, Inc. (b) FEs of H_2, C_1, and C_{2+} products on Cu/C, CuPb–0.7/C and CuPb–1.5/C catalysts. Reproduced with permission from [109]. Copyright 2021, American Chemical Society. (c) The FEs of H_2, C_1, and C_{2+} products on Cu/ZrO_2 and reference catalysts. Reproduced with permission from [137]. Copyright 2022 Elsevier. (d) FE of CO and CH_4 as a function of the Cu–ZnO NP composition. Reproduced with permission from [57]. Copyright 2019, American Chemical Society. (e) FE for C_2H_4 obtained on different Ag/Cu nanocrystals. Reproduced with permission from [104]. Copyright 2019, American Chemical Society. (f) Potential-dependent FEs of C_2H_4 on CuZn alloy catalyst and other samples. Reproduced with permission from [82]. Copyright 2018, American Chemical Society. (g) FEs of different products on CuO/Al_2CuO_4 catalysts. Reproduced with permission from [135]. Copyright 2022, The Royal Society of Chemistry. (h) FEs of the products for a-CuTi@Cu electrocatalyst and commercial Cu and a-CuTi at a potential of −0.8 V_{RHE}. Reproduced with permission from [234]. Copyright 2021, John Wiley & Sons, Inc. (i) FE toward formate and ethanol on Cu_3Sn and Cu_6Sn_5 catalysts. Reproduced with permission from [227]. Copyright 2022, John Wiley & Sons, Inc. (j) FEs of CO reduction on planar and porous CuAg catalysts. Reproduced with permission from [48]. Copyright 2020, National Academy of Sciences. (k) FE of acetate on $(Cu)_2,(Ag)_3$/polymer catalyst. Reproduced with permission from [87]. Copyright 2018, National Academy of Sciences (color online).

sirable to achieve the selectivity toward a particular or a certain category of products as high as possible. Therefore, hydrocarbons and oxygenated compounds enhanced on bimetallic catalysts will be discussed next.

4.3.1   Hydrocarbons
Hydrocarbons account for the major deep reduction products in eCO_2RR, mainly including CH_4, C_2H_4, and trace amount of ethane (C_2H_6). The improved selectivity of CH_4 and C_2H_4 has been frequently observed on bimetallic catalysts consisting of Cu and M_{CO} metals. The hydrocarbon products monitored by the on-line electrochemical mass spectrometry showed the selectivity shift from C_2H_4 to CH_4 by increasing the thickness of the Cu shell on the Au core [67]. CH_4 becomes the main hydrocarbons on Cu metals at relatively negative potential. The metallic Cu with adjacent ZnO was suggested to be crucial for promoting the formation of CH_4 on Cu–Zn bimetallic nanoparticles, while the evolved CuZn alloy shifted the selectivity to CO and H_2 in eCO_2RR (Figure

13d) [57]. Zhang and co-workers [84] exploited the tandem catalysis using a well-defined Cu-modified Ag foil electrode for eCO_2RR and achieved a high CH_4 FE of ~60% at −1.1 V_{RHE} with the optimal surface Cu coverage. At relatively low *CO coverage, Wang and co-workers [83] revealed that the incorporation of Au into Cu matrix facilitated the protonation of *CO and the formation of CH_4 using diluted CO_2 feeding. The reduced *CO coverage on Au–Cu surface was found to favor CH_4 pathway rather than C–C coupling, resulting in a high CH_4 FE of 56% at large current density. From the perspective of the mechanism, the protonation of *CO to *CHO is crucial for CH_4 production in eCO_2RR. The introduction of Pt, an active HER metal, with Cu was able to facilitate the protonation of *CO and promote CH_4 production. However, the stability of Cu–Pt bimetallic catalyst was poor in eCO_2RR, which is possibly due to the adsorbed *CO-induced segregation of Pt [68,210].

C_2H_4 is ideal reduction product from eCO_2RR due to the high market price and huge market demand [211]. Besides,

C_2H_4 often account for the major C_{2+} products that has been produced with a high selectivity at industry-relevant current density [212]. Cu-based bimetallic catalysts are promising candidates for achieving high C_2H_4 FE in eCO_2RR. Feng and co-workers [82] adopted the pulsed laser ablation method to prepare a homogenous CuZn catalyst, where the uniform distribution of Cu and Zn atoms in the CuZn alloy catalysts was important to fulfill the efficient CO transfer from the CO-producing sites (Zn) to Cu sites. With an appropriate Cu/Zn ratio, C_2H_4 FE of about 33.2% was achieved on the homogenous CuZn catalyst. As for the Ag–Cu, the segregated Ag and Cu phases and the interface between them were proposed to play a key role in the enhanced activity and selectivity of C_2H_4 product. The tandem and electronic effects in Ag–Cu nanodimers with tunable interface exhibited a 3.4-fold increase of C_2H_4 FE relative to pure Cu (Figure 13e) [104]. In recent years, the combination of Cu and Al has demonstrated tremendous potential in eCO_2RR to yield a high C_2H_4 activity and selectivity, either forming Cu–Al alloy or composites with Al-containing oxides. Motivated by DFT calculations and machine learning, Cu–Al bimetallic catalyst was identified as the most promising candidate among various bimetallic systems based on the CO binding energy. As a result, the dealloyed nanoporous Cu–Al catalyst reached high C_2H_4 FE of 80% at a large current density (Figure 13f) [117]. Apart from the alloy catalyst, the bimetallic catalysts with abundant Cu–metal oxide interfaces have been recently reported to be highly active for C_2H_4 production in eCO_2RR [134]. The interfaces between CuO and Al_2CuO_4 stabilized the oxidation state of Cu under eCO_2RR condition and enhanced the adsorption and coupling of *CO, resulting in a C_2H_4 FE up to 82.4% in a flow-cell electrolyzer (Figure 13g) [135]. Similarly, the interface between CuO and CeO_2 also stabilized Cu^+ active sites during eCO_2RR, boosting C_2H_4 FE by more than doubled in contrast to pure CuO [132].

Experimentally, it has been observed that the selectivity trends of hydrocarbons and oxygenates on Cu–M_{CO} bimetallic catalysts are often quite different from those on Cu-based catalysts [71,88], The former often witnesses the increase in the FE of oxygenates, while the latter usually shows predominant hydrocarbons over oxygenates in eCO_2RR. For instance, the enhanced selectivity of oxygenates at the cost of ethene was also observed by Clack and co-workers [63] who attributed this phenomenon to the reduced binding energies of H and O caused by the compressive strain in surface Cu–Ag alloys. Similarly, the current density ratio between ethylene and ethanol could be adjusted by the Au content in the AuCu alloy nanoparticles, because the introduction of Au tuned the binding energies of the key intermediates that govern the pathways to ethylene and ethanol [213]. The coverage of *CO and *H was suggested to play an important role in the dimerization rate and hydrogenation rate [61].

Therefore, Lum and co-workers [77] proposed that a high *H coverage was required for the formation of ethylene, while the increased *CO coverage by the CO spillover was postulated to be responsible for the promoted oxygenates production.

It has been demonstrated experimentally and theoretically that hydrocarbons and oxygenates share some key intermediates in eCO_2RR. Although the common intermediate is not yet conclusive, the branched selectivity is closely related to the stabilization of the intermediates on the catalyst surface. By DFT calculations, the *CHO formed by the hydrogenation of adsorbed *CO was proposed to be a key intermediate for the formation of methane and ethane on the Cu surface [170,214]. However, Nie and co-workers [215] proposed that the manners of *CO intermediate hydrogenation drive the pathway to either hydrocarbons (methane and ethylene) or methanol. The proton bonded to C atoms in *CO formed a *CHO intermediate, leading to the formation of methanol. However, the proton bonded to O atoms in *CO formed a *COH intermediate, leading to the formation of methane and ethane. Therefore, the increase in alcohol production was attributed to the facilitated *CHO formation on Cu–ZnO catalysts [216]. The CH_2CHO* intermediate was also suggested to be the selectivity-determining intermediate for oxygenates (acetaldehyde and ethanol) and ethylene. However, the formation of ethylene from this intermediate was more energetically favorable than that of ethanol, explaining the experimental observation that ethylene is the major C_2 product on Cu-based catalysts [11,20,217]. For Cu–M_{CO} bimetallic catalyst, DFT calculation demonstrated that the formation of ethanol from CH_2CHO* was much easier on $Cu_3Au(100)$ surface than on Cu(100), which was consistent with experimental result [213]. The *HCCOH intermediate has also been proposed to be a common intermediate for ethanol and ethylene [218]. The intermediates next to *HCCOH are *CCH and *HCCHOH, leading to the formation of ethylene and ethanol, respectively. Based on this mechanism, it was found that introducing Ag on the Cu surface could disrupt the ethylene pathway more significantly than ethanol pathway, leading to the enhanced ethanol production [71]. Interestingly, Lum and co-workers [219] recently suggested that the ethanol formation has two distinct pathways by conducting CO electroreduction in $H_2^{18}O$ solvent. Likewise, both ethanol pathways overlapped with the ethylene pathway. One pathway branched away from ethylene pathway at *HCCOH intermediate and the other pathway branched away from ethylene pathway at *CCH intermediate. Alternatively, an insertion mechanism was also proposed for the formation of oxygenates in eCO_2RR [220,221]. According to this mechanism, the CO generated on either Zn sites [89], or Ag sites [87,88], spilled over and reacted with *CH_2 intermediate on Cu sites to form a *$COCH_2$ intermediate, which eventually converted to ethanol or acetate. In summary, despite the complex and un-

certain mechanism, these results are beneficial for the understanding of the selectivity trends of hydrocarbons and oxygenates and provide the insight into the ways to modulate the selectivity.

4.3.2 Oxygenates

Compared with hydrocarbons, oxygenates are minor deep-reduction products in eCO_2RR. The bimetallic catalysts with enhanced selectivity of oxygenates convert CO_2 into liquid products with high value, and the studies on them deepen the understanding of the mechanism and structure–activity relationship for oxygenates.

(1) Oxygenates: alcohols

Alcohols, including CH_3OH, C_2H_5OH, and C_3H_7OH, are highly competitive products in eCO_2RR. The bimetallic catalysts consisting of M_{CO} metals and Cu are extensively studied for enhanced alcohols. It has been demonstrated that Cu and ZnO are key components of the catalysts for the application of CO_2 hydrogenation to methanol [222]. Therefore, the couple of Cu and Zn is worth to explore to facilitate the alcohol production in eCO_2RR. Compared with the Cu(111) electrode, the FEs of CH_3OH and ethanol were improved by over one order of magnitude on Cu nanoclusters-modified ZnO electrodes [216]. The FE ratio of C_2H_5OH/C_2H_4 was found to be dependent on the Zn content in the oxide-derived Cu–Zn bimetallic catalysts, and the highest FE of C_2H_5OH reached 29.1% on Cu_4Zn catalysts [89]. Apart from Zn, Au and Ag have also been coupled with Cu to improve the production of alcohols. The introduction of Ag into Cu triggered the electron transfer from Cu to Ag, resulting in electron-deficient Cu sites that favored the C_2H_5OH pathway rather than C_2H_4 [223]. Compared with pure Cu counterpart, Jia and co-workers [224] reported that the electrochemically deposited Cu–Au alloy electrode exhibited a significant increase in FEs of CH_3OH and C_2H_5OH, where Au component was believed to play a key role. Several key factors are proposed to be important for realizing enhanced production of alcohols on bimetallic catalysts. Shen and co-workers [213] prepared a AuCu alloy nanoparticles-decorated Cu arrays that exhibited enhanced FE of C_2H_5OH as the cost of FE of C_2H_4. The selectivity toward ethanol and C_2H_4 was found to be dependent on the Au contents and the highest FE of C_2H_5OH up to 29±4% was achieved due to the abundant AuCu alloy nanoparticles formed on the surface. Except for the atomic ratio, the morphology effect of Cu–Au nanowire arrays also promoted the eCO_2RR to ethanol by increasing the local pH and CO concentration, which benefited the C–C coupling [225]. The proper way in which M_{CO} and Cu are mixed is also important for improving the ethanol selectivity. By changing the deposition solvents, two Ag–Cu bimetallic catalysts with separated and blended phases were obtained. The highest FE of C_2H_5OH reached 34.15% on phase-blended Ag–Cu_2O,

which could be attributed to the higher surface Ag content and abundant Ag–Cu biphasic boundaries [88]. The electrolyte also played a role in determining the selectivity of bimetallic catalysts in eCO_2RR. The Pd–Cu aerogel catalyst showed FE of CH_3OH as high as 80% in ionic-liquid-based solution, while only H_2 and formate were produced in conventional bicarbonate electrolytes [226]. Interestingly, some recent studies demonstrated that high FE of C_2H_5OH could be obtained on Cu–Sn bimetallic catalysts (Figure 13h) [120,227], which often exhibited a high CO selectivity in previous reports.

It has been often observed that the enhanced selectivity toward C_2H_5OH is accompanied with the decreased FE of C_2H_4. This phenomenon strongly suggests that these two predominant C_{2+} products share a common intermediate and their pathways bifurcate at this selectivity-determining intermediate (SDI) after C–C coupling [20,223,228]. It was suggested that the highly coordinated Cu surface facilitated the production of C_2H_4, while the undercoordinated Cu surface with the reduced Cu–Cu coordination number was favorable for C_2H_5OH. The doping of Ag on Cu surfaces was proposed to disrupt the coordinative Cu surface and create diverse binding sites that made for a high FE of C_2H_5OH up to 41% with a current density of 250 mA cm^{-2} at −0.67 V_{RHE} in 1 mol L^{-1} KOH electrolyte [71]. Generally, CO is a key intermediate for C–C coupling toward C_{2+} products. The CO electroreduction on Ag-doped Cu catalysts exhibited a FE of *n*-propanol as high as 33±1%. The Ag doping was proposed to create asymmetric C–C coupling active sites on Cu surface by strain and ligand effects, which promoted the C_1–C_1 and C_1–C_2 coupling [98]. Similarly, the introduction of Ag tailored the surface coordination and oxidation of Cu, providing asymmetric C–C coupling sites for the stabilization of C_2H_5OH intermediate [229]. Recently, the author reported an improved FE of C_2H_5OH with decreased FE of C_2H_4 on a series of Cu–Sn bimetallic catalysts. The incorporated Sn in Cu enhanced the surface oxophilicity, which stabilized the oxygen-containing SDI and guided the pathway to C_2H_5OH [120].

It has been demonstrated that the selectivity among C_{2+} products can be regulated by tuning the CO coverage near the catalyst surface. Relatively low CO coverage is favorable for the stability of C_2H_4-related intermediates, while higher CO coverage is favorable for the formation of oxygen compounds [81]. Placing a CO-producing source in close proximity to Cu catalyst gave rise to a high local CO concentration, which increased the oxygenate to C_2H_4 ratio [77]. Therefore, the tandem mechanism or CO spillover are efficient ways for improving the selectivity to C_{2+} alcohols on bimetallic catalysts. Morales-Guio and co-workers [91] decorated Au nanoparticles on polycrystalline Cu foil by physical vapour deposition. It was found that Au/Cu bimetallic electrodes lowered the overpotential for C_{2+} alcohols,

which was mainly attributed to the enriched local CO concentration on Cu sites (Figure 13i). The enhanced local CO concentration or *CO coverage are considered to be the key to promoting oxygen-containing compound pathways in eCO$_2$RR. The transport of CO generated from Ag to Cu has been investigated by the simulation and experiment using a cascade catalysis model consisting of two parallel-placed Ag and Cu electrodes. The upstream Ag electrodes produced supersaturated CO at downstream Cu electrodes, leading to improved oxygenate products and increased oxygenate to C$_2$H$_4$ ratio [230].

The bimetallic system of Cu–Ag is frequently studied for improving alcohol selectivity in eCO$_2$RR, which is likely due to the immiscibility of Cu and Ag at room temperature. The separated phases with close contact are favorable for realizing the tandem catalysis. The mixture of Ag nanospheres and Cu nanocubes was found to always increase the C$_2$H$_5$OH/C$_2$H$_4$ ratio regardless of the size of Cu nanocubes [156]. Similarly, oxide-derived Cu nanowires mixed with Ag nanoparticles [231]. A moderate amount of Cu-covered Ag nanowires were able to enhance the selectivity to C$_2$H$_5$OH at the expense of C$_2$H$_4$ through an insertion mechanism of spilled-over CO from exposed Ag. However, a large amount of Cu coverage shows pure Cu-like selectivity, mainly through CO dimerization to produce ethylene [232]. The oxide-derived AgCu foam featured highly dispersed Ag domains that contact intimately with Cu matrix, which enabled the efficient CO spillover and was then reduced to C$_2$H$_5$OH by Cu species [85]. From the perspective of mechanism, some studies demonstrated that the promotion of alcohol selectivity *via* the tandem catalysis can be understood by an insertion mechanism. Different from the C$_2$H$_4$ production from the C–C coupling between *CO and *CO or *CHO, the CO generated at M$_{CO}$ sites transferred and coupled with adsorbed *CH$_x$ species at Cu sites, leading to the pathways toward oxygenate products [88,89,233].

(2) Oxygenates: aldehyde and acetate

Compared with ethanol, acetaldehyde and acetate products are less reported oxygenates with lower FE in eCO$_2$RR. Similar to alcohols, the production of aldehyde and acetate is highly related to the enriched local CO concentration. Using CO as feeding gas, Wang and co-workers [48] achieved a FE of acetaldehyde as high as 70% on the galvanically replaced AgCu electrode, demonstrating the importance of CO intermediate for further reduction (Figure 13j). Lum and co-workers [77] fabricated a bimetallic device consisting of separated Au and Cu micropatterns. The CO spillover across micron-scale was verified by both simulation and experiment. The CO produced on the Au lines could transfer to the Cu lines and be further reduced to oxygenates, among which the selectivity of acetate and acetaldehyde enhanced significantly compared with pure Cu. Similarly, the novel assembly of Au nanoparticles (NPs) and Cu nanowires (NWs)

connected by 4,4′-bipyridine exhibited a high FE of aldehyde of 25% in eCO$_2$RR, where the tandem effect between Au and Cu and 4,4′-bipyridine ligand jointly contributed to such selectivity [235]. Obviously, the enhanced FE of acetaldehyde and acetate is often realized on Cu-based bimetallic catalysts. However, the mechanisms and factors that promote the selectivity of acetaldehyde and acetate rather than alcohols are still unclear. The addition of 8 ppm of benzotriazole in the 0.5 mol L^{-1} KHCO$_3$ electrolyte was reported to play a key role in achieving a FE of acetate up to 21.2% on ultrasmall Cu–Ag bimetallic nanoparticles in eCO$_2$RR (Figure 13k) [87]. Rather than the effect of CO spillover, Clark and co-workers [63] attributed the enhanced selectivity toward acetaldehyde and acetate to the change of electronic structure and oxophilicity caused by the compressive strain on Cu–Ag surface alloy.

4.4 Rules of selectivity for bimetallic combination

One of the most mysterious parts of the bimetallic catalysts for eCO$_2$RR is their selectivity. For instance, significant improvement toward different reduction products has been reported on Cu–Au bimetallic systems, including CO [119], formate [236], hydrocarbons [83], oxygenates [77,213], and total C$_{2+}$ products [78]. The same story also happens on other bimetallic systems, such as Cu–Ag and Cu–Sn. On one hand, the broad product distribution on Cu results in the various selectivity of Cu-containing bimetallic catalysts. On the other hand, a slight difference in the structure and atomic arrangement can make a significant different in the selectivity of bimetallic catalysts, even with similar metal combination.

However, through the survey of the eCO$_2$RR performance of bimetallic catalysts (Table 1), several rules of the selectivity trends of bimetallic catalysts in eCO$_2$RR can be summarized.

(1) Combinations of metals within the same group often remain the selectivity characteristic, but with improvement. Through the synergy or interface of the two metals, the eCO$_2$RR performance of these bimetallic catalysts often exceeds that of the corresponding single-component counterparts, such as Zn–Ag and Bi–Sn [125,162].

(2) Pd is a unique metal in eCO$_2$RR, exhibiting predominate 2e product. The bimetallic catalysts containing Pd often show the enhanced selectivity and activity toward 2e products, including both CO and formate [181,200]. However, when combined with Cu, various reduction products can be produced, such as CO, formate, CH$_4$, CH$_3$OH, and C$_{2+}$ [184,201,209,226,239,240].

(3) Cu-containing bimetallic catalysts inherit the selectivity of Cu in eCO$_2$RR, making Cu the necessary component of bimetallic catalysts for producing deep-reduction products. On the other hand, the uniqueness of Cu in bimetallic cata-

Table 1   The representative bimetallic catalysts and their catalytic performance in eCO$_2$RR

Catalyst	Main product	Faradaic efficiencies	Partial current density	Stability test	Ref.
ZnO–Ag@UC	CO	94.1±4.0%@−0.93 V$_{RHE}$	22.3 mA cm^{-2}@−0.93 V$_{RHE}$	150 h@−0.93 V$_{RHE}$	[162]
AgCu SAA	CO	97.5%@−0.91 V$_{RHE}$	0.72 μA cm^{-2}@−0.41 V$_{RHE}$	13 h@−0.91 V$_{RHE}$	[237]
AuCu$_3$@Au	CO	97.27%@−0.6 V$_{RHE}$	5.3 mA cm^{-2}@−0.6 V$_{RHE}$	100 h@−0.7 V$_{RHE}$	[100]
Ordered AuCu NPs	CO	~80%@−0.77 V$_{RHE}$	1.39 mA cm^{-2}@−0.77 V$_{RHE}$	12 h@−0.76 V$_{RHE}$	[119]
CuO–0.4%Sn	CO	98%@−0.75 V$_{RHE}$	~1.6 mA cm^{-2}@−0.75 V$_{RHE}$	15 h@−0.75 V$_{RHE}$	[145]
CuIn20	CO	~93%@−0.6 V$_{RHE}$	~1.7 mA cm^{-2}@−0.6 V$_{RHE}$	60 h@−0.6 V$_{RHE}$	[73]
Pd$_{0.8}$Au nanowire	CO	94.3%@−0.6 V$_{RHE}$	2.77 mA cm^{-2}@−0.6 V$_{RHE}$	8 h@−0.6 V$_{RHE}$	[181]
GDE–In$_{0.90}$Sn$_{0.10}$	Formate	~92%@−1.2 V$_{RHE}$	~13.8 mA cm^{-2}@−1.2 V$_{RHE}$	22 h@-1.2 V$_{RHE}$	[188]
Bi–Sn aerogel	Formate	~93.9%@−1.0 V$_{RHE}$	9.3 mA cm^{-2}@−1.0 V$_{RHE}$	10 h@−1.0 V$_{RHE}$	[125]
PdSn/C	Formate	>99%@−0.43 V$_{RHE}$	~1.8 mA cm^{-2} @−0.43 V$_{RHE}$	5 h@−0.43 V$_{RHE}$	[200]
Cu$_2$SnS$_3$	Formate	80.1%@−1.1 V$_{RHE}$	64.6 mA cm^{-2}@−1.1 V$_{RHE}$	10 h@−1.0 V$_{RHE}$	[238]
Ag/Cu	C$_2$H$_4$	42%@−1.1 V$_{RHE}$	2.31 mA cm^{-2}@−1.1 V$_{RHE}$	30 h@−1.1 V$_{RHE}$	[79]
Ag$_1$–Cu$_{1.1}$ NDs	C$_2$H$_4$	~40%@−1.1 V$_{RHE}$	/	/	[104]
Cu$_{70}$Zn$_{30}$	CH$_4$	70.2%@−1.35 V$_{RHE}$	~37 mA cm^{-2}@−1.35 V$_{RHE}$	5 h@−1.35 V$_{RHE}$	[57]
CuAu	C$_{2+}$	~70%@−1.05 V$_{RHE}$	~30 mA cm^{-2}@−1.05 V$_{RHE}$	/	[78]
Cu$_5$Zn$_8$	C$_2$H$_5$OH	46.6%@−0.8 V$_{RHE}$	2.3 mA cm^{-2}@−0.8 V$_{RHE}$	11 h@−0.8 V$_{RHE}$	[58]
CuZn core–shell	C$_2$H$_5$OH	32%@−1.15 V$_{RHE}$	10.5 mA cm^{-2}@−1.15 V$_{RHE}$	/	[233]
Cu$_x$Au$_y$ NWAs	C$_2$H$_5$OH	~45%@−0.7 V$_{RHE}$	1 mA cm^{-2}@−0.7 V$_{RHE}$	8 h@−0.7 V$_{RHE}$	[225]
Au–bipy–Cu	CH$_3$CHO	25%@−0.9 V$_{RHE}$	~3.25 mA cm^{-2}@−0.9 V$_{RHE}$	6 h@−0.9 V$_{RHE}$	[235]

lysts is also reflected by its versatility, as nearly all eCO$_2$RR reduction products can be enhanced by Cu-containing bimetallic catalysts. Although the eCO$_2$RR performance of Cu-based catalysts can often be improved by the bimetallic strategy, the selectivity trends of the combination of Cu and other groups of metals are complicated and hard to be predicted. High selectivity toward 2e products can be expected on Cu-containing bimetallic catalysts in conjunction with M$_{CO}$ and M$_{HCOOH}$. By increasing the local CO concentration *via* the tandem mechanism, it is possible to improve the formation of oxygenates. The electronic effect in bimetallic alloys or the interfacial effect in heterostructured bimetallic catalysts are often considered for increasing the selectivity toward hydrocarbons. In addition to the common metals used for eCO$_2$RR, some metals that show almost no activity in eCO$_2$RR have been recently coupled with Cu for improving the performance of eCO$_2$RR, such as Mg, Al, and Ti [117,234,241].

(4) Apart from the metal components that show activity toward eCO$_2$RR, some uncommon bimetallic combinations that exhibit unique eCO$_2$RR performance are also worth studying for understanding the nature of bimetallic catalysts in eCO$_2$RR. Nickel-based bimetallic films have been reported to be capable of electrochemically reducing CO$_2$ into deep-reduction products, such as Ni–Ga and Ni–Al [242,243]. High FEs of CH$_3$OH and C$_2$H$_5$OH were achieved on the *n*-GaAs electrode and AgCo alloy, respectively [244,245].

5   Summary and outlook

Coupling eCO$_2$RR with a renewable energy source to produce valuable fuels and chemicals using CO$_2$ and H$_2$O is a promising strategy for achieving a sustainable energy economy. The catalyst is the important foundation and prerequisite for the scale-up of eCO$_2$RR process. Bimetallic strategy holds the great promise in the development of high-efficiency catalysts for eCO$_2$RR. In this Review, we took a comprehensive look at the state of eCO$_2$RR on bimetallic catalysts. The key mechanisms that have been used to tune the activity and selectivity of eCO$_2$RR have been initially discussed, which is the foundation of understanding the catalytic performance on bimetallic catalysts. The function of various effects in bimetallic catalysts is highly dependent on the microstructure of bimetallic catalysts. Therefore, the structural design of bimetallic catalysts for eCO$_2$RR was then discussed in this review, which provides the instruction for the design of bimetallic catalysts for eCO$_2$RR. Finally, the advances of bimetallic catalysts for eCO$_2$RR were discussed in terms of the product selectivity and some rules of the selectivity were concluded.

Although substantial advances have been achieved on bimetallic catalysts in eCO$_2$RR, there are still challenges and opportunities in this direction. Various synthesis approaches have been developed to construct bimetallic catalysts for eCO$_2$RR. The combination of metals also increases the complexity of the active sites on the surfaces of bimetallic

catalysts. It is still a formidable task to identify the active sites with high catalytic performance and understand the origin of such activity in bimetallic catalysts. On the other hand, the precise and controllable synthesis of bimetallic active sites at atomic scale is still of great challenge. There is a lack of model catalysts to investigate the promotion mechanism for eCO$_2$RR of bimetallic catalysts. Furthermore, most of the present studies rely on the trial-and-error to discover high-efficiency bimetallic catalysts for eCO$_2$RR. New research paradigm combining high throughput synthesis, catalyst evaluation, and theoretical screening is a promising way to accelerate the development of bimetallic catalysts for eCO$_2$RR.The efforts in the following direction may further advance the bimetallic catalysts for eCO$_2$RR.

(1) Inspired by the achievements of bimetallic catalysts in eCO$_2$RR, increasing the component in the catalysts is expected to diversify the binding sites and create more under-coordinated metal sites, which significantly affects the binding of intermediates and the reaction pathways for eCO$_2$RR. He and co-workers [246] reported a ternary Cu$_{0.2}$Zn$_{0.4}$Sn$_{0.4}$ catalyst that exhibited a high activity and selectivity toward CO in eCO$_2$RR at the low overpotential of only 200 mV, which was superior to binary alloys. The increase in the composition of catalysts could also integrate the favorable effects for improved eCO$_2$RR performance. The ternary Cu$_3$–Ag$_3$Au nanoframes showed a high C$_2$H$_4$ production *via* the tandem effect, *i.e.*, the electronic effects between separated Ag/Au and Cu domains [27]. Recently, high-entropy alloys (HEAs) consisting of more than five metals have been drawing increasing attention in the field of electrocatalysts [247]. Numerous binding sites can be created on the surface of HEAs, opening various possibilities for eCO$_2$RR. In 2020, Nellaiappan and co-workers [248] first adopted HEAs-based catalysts in eCO$_2$RR. Noteworthily, the equiatomic Au–Ag–Pt–Pd–Cu HEA-based catalyst showed the nearly 100% selectivity toward gaseous products with high FEs of hydrocarbons, including CH$_4$ and C$_2$H$_4$. However, the employment of HEAs as electrocatalysts for eCO$_2$RR is still in the infant stage. Motivated by the uniqueness of Cu-based catalytic property in eCO$_2$RR, Pedersen and co-workers [249] utilized the criteria of weak H adsorption and strong CO adsorption to optimize the composition of HEAs for discovering candidates for eCO$_2$RR. Recently, a PdCuAuAgBiIn HEA aerogel was synthesized and exhibited nearly 100% FE toward C$_1$ products with predominant formate in eCO$_2$RR. The electronic interactions among different metal atoms and undercoordinated surface sites effectively regulated the adsorption strength of intermediates [250]. It has been demonstrated that various metals exhibit outstanding activities in eCO$_2$RR or serve as efficient promotors for bimetallic catalysts. Therefore, beyond bimetallic catalysts, there will be a variety of selections for multicomponent catalysts, which hold the promise of achieving high eCO$_2$RR

performance.

(2) From section 4, it is known that a variety of metal elements could be used for constituting bimetallic catalysts for eCO$_2$RR, including the ones with and without activities toward eCO$_2$RR. The selection of metal combination is still the paramount question when designing bimetallic catalysts for eCO$_2$RR. Experimentally, high-throughput screening of catalysts is necessary and efficient for discovering the optimal bimetallic combination for eCO$_2$RR. High-throughput screening of bimetallic catalysts for eCO$_2$RR requires sound synthesis methods to synthesize a broad range of bimetallic catalysts with similar morphology and structure as well as controllable stoichiometry. He and co-workers [251] reported a series of In-based bimetallic catalysts synthesized by the near-infrared-light-driven decomposition method for the high-throughput synthesis and screening of bimetallic catalysts for eCO$_2$RR. A series of Cu-based homogeneous alloys could be obtained regardless of the thermodynamic miscibility by a nonequilibrium synthesis method based on the rapid thermal shock process. Among them, the Cu$_{0.9}$Ni$_{0.1}$ bimetallic catalyst showed the best catalytic performance of carbon monoxide electroreduction [208]. On the other hand, a setup of fast catalyst-screening platform could help accelerate the evaluation of eCO$_2$RR performance on a large number of bimetallic catalysts. A quasi-automatic platform for the fast screening of bimetallic catalysts for eCO$_2$RR has been recently reported, which consists of a control program, a flow eCO$_2$RR cell, a screw slide platform, and an online micro-fast gas chromatograph. This system was able to complete the eCO$_2$RR performance evaluation of each bimetallic catalyst within 3 min. Based on 942 tests finished in 55 working hours, the Mg–Cu catalyst stood out as the best combination for C$_{2+}$ production among 109 Cu-based bimetallic catalysts [241]. Therefore, the establishment of high-throughput synthesis and screening approach is of great significance for the development of bimetallic catalysts for eCO$_2$RR.

(3) The investigation of the reaction paths for various reduction products has always been the focus of research in the field of eCO$_2$RR. The thorough understanding of reaction mechanism is a prerequisite for the rational design of catalysts. Theoretical calculation is an important tool that provides theoretical guidance for experimental studies. The reaction details and energetics of elementary reactions can be provided by theoretical studies. In order to understand the catalytic performance of eCO$_2$RR reactions on bimetallic catalysts, DFT calculations are often used to interpret experimental observations. On the other hand, the theoretical calculations can also guide the design of bimetallic catalysts by predicting their catalytic performance based on the binding properties to key intermediates in eCO$_2$RR [252].

(4) There are many potential eCO$_2$RR active sites in binary and multi-component metallic catalysts due to the differ-

ences in composition, crystal orientation and surface atomic arrangement. Experimentally, it is almost an impossible task to screen out the optimal metal combination and identify the structure of advantageous active sites for eCO$_2$RR. DFT calculations are known for directly acquiring adsorption properties on the catalysts, which cannot be measured experimentally [253]. However, it is a formidable and time-consuming task to perform DFT calculations on tremendous active sites on various bimetallic catalysts. Therefore, combining DFT calculation with active machine learning holds the promise to realize the high-throughput screening of bimetallic catalysts for eCO$_2$RR in the framework of binding strength [254]. The catalyst screening by machine learning-augmented DFT studies is usually based on the binding energies of eCO$_2$RR-related absorbents. Ma and co-workers [255] developed a machine-learning model that integrated artificial neural networks and DFT calculations, which identified two promising multimetallic candidates for C$_{2+}$ production in eCO$_2$RR based on the CO adsorption energy. Using quantum mechanics rapid screening, Au–Fe was identified as the best alloy candidates for converting CO$_2$ into CO [40]. Similarly, combining DFT calculations with active machine learning, the Cu–Al bridge sites in the Cu-rich environment on the Cu–Al alloy surface was predicted to be active for the further reduction of *CO due to the near optimal CO binding energy [117]. Compared with trial-and-error laboratorial investigation, the integrated theoretical study and machine learning undoubtedly accelerate the screening and guide the rational synthesis of bimetallic catalysts for eCO$_2$RR. Apart from the extensively concerned eCO$_2$RR activity and selectivity, the stability of bimetallic catalysts is also important trait for eCO$_2$RR and should be studied and predicted by machine learning models trained by DFT calculations.

Finally, from the economic and industrial perspectives, the bimetallic strategy also holds great promise for eCO$_2$RR process. The precious metals are still an excellent choice for industrial applications of eCO$_2$RR due to their outstanding selectivity at low overpotential. Bimetallic strategies can significantly reduce the cost of precious metals and substantially improve the mass activity. Furthermore, at the industry-relevant current density, various bimetallic catalysts have been reported to show excellent eCO$_2$RR-catalytic performance, demonstrating their huge potentials for the further application.

Conflict of interest   The authors declare no conflict of interest.

1   Li M, Wang H, Luo W, Sherrell PC, Chen J, Yang J. *Adv Mater*, 2020, 32: 2001848

2   Vasileff A, Xu C, Jiao Y, Zheng Y, Qiao SZ. *Chem*, 2018, 4: 1809–1831

3   Deng B, Zhao X, Li Y, Huang M, Zhang S, Dong F. *Sci China Chem*, 2022, 66: 78–95

4   Han N, Ding P, He L, Li Y, Li Y. *Adv Energy Mater*, 2019, 10: 1902338

5   Birhanu MK, Tsai MC, Kahsay AW, Chen CT, Zeleke TS, Ibrahim KB, Huang CJ, Su WN, Hwang BJ. *Adv Mater Interfaces*, 2018, 5: 1800919

6   Hori Y, Kikuchi K, Suzuki S. *Chem Lett*, 1985, 14: 1695–1698

7   Hori Y, Kikuchi K, Murata A, Suzuki S. *Chem Lett*, 1986, 15: 897–898

8   Liu S, Sun C, Xiao J, Luo JL. *ACS Catal*, 2020, 10: 3158–3163

9   Yang F, Elnabawy AO, Schimmenti R, Song P, Wang J, Peng Z, Yao S, Deng R, Song S, Lin Y, Mavrikakis M, Xu W. *Nat Commun*, 2020, 11: 1088

10   Zhang G, Zhao ZJ, Cheng D, Li H, Yu J, Wang Q, Gao H, Guo J, Wang H, Ozin GA, Wang T, Gong J. *Nat Commun*, 2021, 12: 5745

11   Kortlever R, Shen J, Schouten KJP, Calle-Vallejo F, Koper MTM. *J Phys Chem Lett*, 2015, 6: 4073–4082

12   McKenzie ECR, Hosseini S, Petro AGC, Rudman KK, Gerroll BHR, Mubarak MS, Baker LA, Little RD. *Chem Rev*, 2021, 122: 3292–3335

13   Feaster JT, Shi C, Cave ER, Hatsukade T, Abram DN, Kuhl KP, Hahn C, Nørskov JK, Jaramillo TF. *ACS Catal*, 2017, 7: 4822–4827

14   Huang Y, Mao X, Yuan G, Zhang D, Pan B, Deng J, Shi Y, Han N, Li C, Zhang L, Wang L, He L, Li Y, Li Y. *Angew Chem Int Ed*, 2021, 60: 15844–15848

15   Hirunsit P, Soodsawang W, Limtrakul J. *J Phys Chem C*, 2015, 119: 8238–8249

16   Zhan C, Dattila F, Rettenmaier C, Bergmann A, Kühl S, García-Muelas R, López N, Cuenya BR. *ACS Catal*, 2021, 11: 7694–7701

17   Montoya JH, Shi C, Chan K, Nørskov JK. *J Phys Chem Lett*, 2015, 6: 2032–2037

18   Xiao C, Zhang J. *ACS Nano*, 2021, 15: 7975–8000

19   Liu Q, Zhang XG, Du ZY, Zou CJ, Chen HY, Zhao Y, Dong JC, Fang PP, Li JF. *Sci China Chem*, 2023, 66: 259–265

20   Calle-Vallejo F, Koper MTM. *Angew Chem Int Ed*, 2013, 52: 7282–7285

21   Zhu W, Zhang YJ, Zhang H, Lv H, Li Q, Michalsky R, Peterson AA, Sun S. *J Am Chem Soc*, 2014, 136: 16132–16135

22   Klinkova A, De Luna P, Dinh CT, Voznyy O, Larin EM, Kumacheva E, Sargent EH. *ACS Catal*, 2016, 6: 8115–8120

23   Li M, Ma Y, Chen J, Lawrence R, Luo W, Sacchi M, Jiang W, Yang J. *Angew Chem Int Ed*, 2021, 60: 11487–11493

24   Chang X, He M, Lu Q, Xu B. *Sci China Chem*, 2023, 66: 96–106

25   Hansen HA, Varley JB, Peterson AA, Nørskov JK. *J Phys Chem Lett*, 2013, 4: 388–392

26   Zhao ZJ, Liu S, Zha S, Cheng D, Studt F, Henkelman G, Gong J. *Nat Rev Mater*, 2019, 4: 792–804

27   Xiong L, Zhang X, Yuan H, Wang J, Yuan X, Lian Y, Jin H, Sun H, Deng Z, Wang D, Hu J, Hu H, Choi J, Li J, Chen Y, Zhong J, Guo J, Rümmerli MH, Xu L, Peng Y. *Angew Chem Int Ed*, 2020, 60: 2508–2518

28   Peterson AA, Nørskov JK. *J Phys Chem Lett*, 2012, 3: 251–258

29   Ouyang Y, Shi L, Bai X, Li Q, Wang J. *Chem Sci*, 2020, 11: 1807–1813

30   Watanabe M, Shibata M, Katoh A, Sakata T, Azuma M. *J Electroanal Chem Interfacial Electrochem*, 1991, 305: 319–328

31   Watanabe M, Shibata M, Kato A, Azuma M, Sakata T. *J Electrochem Soc*, 1991, 138: 3382–3389

32   Sun L, Reddu V, Wang X. *Chem Soc Rev*, 2022, 51: 8923–8956

33   Parkin A, Seravalli J, Vincent KA, Ragsdale SW, Armstrong FA. *J Am Chem Soc*, 2007, 129: 10328–10329

34   Jovanov ZP, Hansen HA, Varela AS, Malacrida P, Peterson AA, Nørskov JK, Stephens IEL, Chorkendorff I. *J Catal*, 2016, 343: 215–231

35   Zhou JH, Lan DW, Yang SS, Guo Y, Yuan K, Dai LX, Zhang YW.

Inorg Chem Front, 2018, 5: 1524–1532

36 Li M, Wang J, Li P, Chang K, Li C, Wang T, Jiang B, Zhang H, Liu H, Yamauchi Y, Umezawa N, Ye J. *J Mater Chem A*, 2016, 4: 4776–4782

37 Strasser P, Koh S, Anniyev T, Greeley J, More K, Yu C, Liu Z, Kaya S, Nordlund D, Ogasawara H, Toney MF, Nilsson A. *Nat Chem*, 2010, 2: 454–460

38 Kong F, Ren Z, Norouzi Banis M, Du L, Zhou X, Chen G, Zhang L, Li J, Wang S, Li M, Doyle-Davis K, Ma Y, Li R, Young A, Yang L, Markiewicz M, Tong Y, Yin G, Du C, Luo J, Sun X. *ACS Catal*, 2020, 10: 4205–4214

39 Escudero-Escribano M, Verdaguer-Casadevall A, Malacrida P, Grønbjerg U, Knudsen BP, Jepsen AK, Rossmeisl J, Stephens IEL, Chorkendorff I. *J Am Chem Soc*, 2012, 134: 16476–16479

40 Sun K, Cheng T, Wu L, Hu Y, Zhou J, Maclennan A, Jiang Z, Gao Y, Goddard Iii WA, Wang Z. *J Am Chem Soc*, 2017, 139: 15608–15611

41 Dai S, Huang TH, Liu WI, Hsu CW, Lee SW, Chen TY, Wang YC, Wang JH, Wang KW. *Nano Lett*, 2021, 21: 9293–9300

42 Zhu W, Tackett BM, Chen JG, Jiao F. *Top Curr Chem (Z)*, 2018, 376: 41

43 Tackett BM, Lee JH, Chen JG. *Acc Chem Res*, 2020, 53: 1535–1544

44 Lee CW, Yang KD, Nam DH, Jang JH, Cho NH, Im SW, Nam KT. *Adv Mater*, 2018, 30: 1704717

45 He J, Johnson NJJ, Huang A, Berlinguette CP. *ChemSusChem*, 2018, 11: 48–57

46 Wang H, Gu XK, Zheng X, Pan H, Zhu J, Chen S, Cao L, Li WX, Lu J. *Sci Adv*, 2019, 5: eaat6413

47 Kim D, Resasco J, Yu Y, Asiri AM, Yang P. *Nat Commun*, 2014, 5: 4948

48 Wang L, Higgins DC, Ji Y, Morales-Guio CG, Chan K, Hahn C, Jaramillo TF. *Proc Natl Acad Sci USA*, 2020, 117: 12572–12575

49 Ross MB, Dinh CT, Li Y, Kim D, De Luna P, Sargent EH, Yang P. *J Am Chem Soc*, 2017, 139: 9359–9363

50 Liu P, Nørskov JK. *Phys Chem Chem Phys*, 2001, 3: 3814–3818

51 Zhang H, Jin X, Lee JM, Wang X. *ACS Nano*, 2022, 16: 17572–17592

52 Rodriguez JA, Goodman DW. *Science*, 1992, 257: 897–903

53 Ma M, Hansen HA, Valenti M, Wang Z, Cao A, Dong M, Smith WA. *Nano Energy*, 2017, 42: 51–57

54 Liu K, Ma M, Wu L, Valenti M, Cardenas-Morcoso D, Hofmann JP, Bisquert J, Gimenez S, Smith WA. *ACS Appl Mater Interfaces*, 2019, 11: 16546–16555

55 Kim JH, Woo H, Yun SW, Jung HW, Back S, Jung Y, Kim YT. *Appl Catal B-Environ*, 2017, 213: 211–215

56 Takashima T, Suzuki T, Irie H. *Electrochim Acta*, 2017, 229: 415–421

57 Jeon HS, Timoshenko J, Scholten F, Sinev I, Herzog A, Haase FT, Roldan Cuenya B. *J Am Chem Soc*, 2019, 141: 19879–19887

58 Su X, Sun Y, Jin L, Zhang L, Yang Y, Kerns P, Liu B, Li S, He J. *Appl Catal B-Environ*, 2020, 269: 118800

59 Liu B, Xie Y, Wang X, Gao C, Chen Z, Wu J, Meng H, Song Z, Du S, Ren Z. *Appl Catal B-Environ*, 2022, 301: 120781

60 Friebel D, Mbuga F, Rajasekaran S, Miller DJ, Ogasawara H, Alonso-Mori R, Sokaras D, Nordlund D, Weng TC, Nilsson A. *J Phys Chem C*, 2014, 118: 7954–7961

61 Sandberg RB, Montoya JH, Chan K, Nørskov JK. *Surf Sci*, 2016, 654: 56–62

62 Morimoto M, Takatsuji Y, Yamasaki R, Hashimoto H, Nakata I, Sakakura T, Haruyama T. *Electrocatalysis*, 2018, 9: 323–332

63 Clark EL, Hahn C, Jaramillo TF, Bell AT. *J Am Chem Soc*, 2017, 139: 15848–15857

64 Chang CJ, Lin SC, Chen HC, Wang J, Zheng KJ, Zhu Y, Chen HM. *J Am Chem Soc*, 2020, 142: 12119–12132

65 Schlapka A, Lischka M, Groß A, Käsberger U, Jakob P. *Phys Rev Lett*, 2003, 91: 016101

66 Li Q, Fu J, Zhu W, Chen Z, Shen B, Wu L, Xi Z, Wang T, Lu G, Zhu J, Sun S. *J Am Chem Soc*, 2017, 139: 4290–4293

67 Monzó J, Malewski Y, Kortlever R, Vidal-Iglesias FJ, Solla-Gullón J, Koper MTM, Rodriguez P. *J Mater Chem A*, 2015, 3: 23690–23698

68 Reske R, Duca M, Oezaslan M, Schouten KJP, Koper MTM, Strasser P. *J Phys Chem Lett*, 2013, 4: 2410–2413

69 Maroun F, Ozanam F, Magnussen OM, Behm RJ. *Science*, 2001, 293: 1811–1814

70 Ma S, Sadakiyo M, Heima M, Luo R, Haasch RT, Gold JI, Yamauchi M, Kenis PJA. *J Am Chem Soc*, 2017, 139: 47–50

71 Li YC, Wang Z, Yuan T, Nam DH, Luo M, Wicks J, Chen B, Li J, Li F, de Arquer FPG, Wang Y, Dinh CT, Voznyy O, Sinton D, Sargent EH. *J Am Chem Soc*, 2019, 141: 8584–8591

72 Sarfraz S, Garcia-Esparza AT, Jedidi A, Cavallo L, Takanabe K. *ACS Catal*, 2016, 6: 2842–2851

73 Luo W, Xie W, Mutschler R, Oveisi E, De Gregorio GL, Buonsanti R, Züttel A. *ACS Catal*, 2018, 8: 6571–6581

74 Hatsukade T, Kuhl KP, Cave ER, Abram DN, Feaster JT, Jongerius AL, Hahn C, Jaramillo TF. *Energy Technol*, 2017, 5: 955–961

75 Xie C, Niu Z, Kim D, Li M, Yang P. *Chem Rev*, 2020, 120: 1184–1249

76 Cao B, Li FZ, Gu J. *ACS Catal*, 2022, 12: 9735–9752

77 Lum Y, Ager JW. *Energy Environ Sci*, 2018, 11: 2935–2944

78 Gao J, Ren D, Guo X, Zakeeruddin SM, Grätzel M. *Faraday Discuss*, 2019, 215: 282–296

79 Wang J, Li Z, Dong C, Feng Y, Yang J, Liu H, Du X. *ACS Appl Mater Interfaces*, 2019, 11: 2763–2767

80 Huang Y, Handoko AD, Hirunsit P, Yeo BS. *ACS Catal*, 2017, 7: 1749–1756

81 Li J, Wang Z, McCallum C, Xu Y, Li F, Wang Y, Gabardo CM, Dinh CT, Zhuang TT, Wang L, Howe JY, Ren Y, Sargent EH, Sinton D. *Nat Catal*, 2019, 2: 1124–1131

82 Feng Y, Li Z, Liu H, Dong C, Wang J, Kulinich SA, Du X. *Langmuir*, 2018, 34: 13544–13549

83 Wang X, Ou P, Wicks J, Xie Y, Wang Y, Li J, Tam J, Ren D, Howe JY, Wang Z, Ozden A, Finfrock YZ, Xu Y, Li Y, Rasouli AS, Bertens K, Ip AH, Graetzel M, Sinton D, Sargent EH. *Nat Commun*, 2021, 12: 3387

84 Zhang H, Chang X, Chen JG, Goddard III WA, Xu B, Cheng MJ, Lu Q. *Nat Commun*, 2019, 10: 3340

85 Dutta A, Montiel IZ, Erni R, Kiran K, Rahaman M, Drnec J, Broekmann P. *Nano Energy*, 2020, 68: 104331

86 Gao J, Zhang H, Guo X, Luo J, Zakeeruddin SM, Ren D, Grätzel M. *J Am Chem Soc*, 2019, 141: 18704–18714

87 Wang Y, Wang D, Dares CJ, Marquard SL, Sheridan MV, Meyer TJ. *Proc Natl Acad Sci USA*, 2018, 115: 278–283

88 Lee S, Park G, Lee J. *ACS Catal*, 2017, 7: 8594–8604

89 Ren D, Ang BSH, Yeo BS. *ACS Catal*, 2016, 6: 8239–8247

90 Tan YC, Lee KB, Song H, Oh J. *Joule*, 2020, 4: 1104–1120

91 Morales-Guio CG, Cave ER, Nitopi SA, Feaster JT, Wang L, Kuhl KP, Jackson A, Johnson NC, Abram DN, Hatsukade T, Hahn C, Jaramillo TF. *Nat Catal*, 2018, 1: 764–771

92 Chen C, Li Y, Yu S, Louisia S, Jin J, Li M, Ross MB, Yang P. *Joule*, 2020, 4: 1688–1699

93 Xiong L, Zhang X, Chen L, Deng Z, Han S, Chen Y, Zhong J, Sun H, Lian Y, Yang B, Yuan X, Yu H, Liu Y, Yang X, Guo J, Rümmeli MH, Jiao Y, Peng Y. *Adv Mater*, 2021, 33: 2101741

94 Zhu C, Zhou L, Zhang Z, Yang C, Shi G, Zhao S, Gu H, Wu J, Gao X, Li Y, Liu K, Dai S, Zhang L. *Chem*, 2022, 8: 3288–3301

95 Yin Z, Yu J, Xie Z, Yu SW, Zhang L, Akauola T, Chen JG, Huang W, Qi L, Zhang S. *J Am Chem Soc*, 2022, 144: 20931–20938

96 Meng DL, Zhang MD, Si DH, Mao MJ, Hou Y, Huang YB, Cao R. *Angew Chem Int Ed*, 2021, 60: 25485–25492

97 Zhang XG, Feng S, Zhan C, Wu DY, Zhao Y, Tian ZQ. *J Phys Chem Lett*, 2020, 11: 6593–6599

98 Wang X, Wang Z, Zhuang TT, Dinh CT, Li J, Nam DH, Li F, Huang CW, Tan CS, Chen Z, Chi M, Gabardo CM, Seifitokaldani A, Todorović P, Proppe A, Pang Y, Kirmani AR, Wang Y, Ip AH, Richter

LJ, Scheffel B, Xu A, Lo SC, Kelley SO, Sinton D, Sargent EH. *Nat Commun*, 2019, 10: 5186

99 Chu S, Hong S, Masa J, Li X, Sun Z. *Chem Commun*, 2019, 55: 12380–12383

100 Ma X, Shen Y, Yao S, An C, Zhang W, Zhu J, Si R, Guo C, An C. *J Mater Chem A*, 2020, 8: 3344–3350

101 Wang L, Peng H, Lamaison S, Qi Z, Koshy DM, Stevens MB, Wakerley D, Zamora Zeledón JA, King LA, Zhou L, Lai Y, Fontecave M, Gregoire J, Abild-Pedersen F, Jaramillo TF, Hahn C. *Chem Catal*, 2021, 1: 663–680

102 Cui M, Johnson G, Zhang Z, Li S, Hwang S, Zhang X, Zhang S. *Nanoscale*, 2020, 12: 14068–14075

103 Adit Maark T, Peterson AA. *J Phys Chem C*, 2014, 118: 4275–4281

104 Huang J, Mensi M, Oveisi E, Mantella V, Buonsanti R. *J Am Chem Soc*, 2019, 141: 2490–2499

105 Shao Q, Wang P, Liu S, Huang X. *J Mater Chem A*, 2019, 7: 20478–20493

106 Varela AS, Schlaup C, Jovanov ZP, Malacrida P, Horch S, Stephens IEL, Chorkendorff I. *J Phys Chem C*, 2013, 117: 20500–20508

107 Luc W, Collins C, Wang S, Xin H, He K, Kang Y, Jiao F. *J Am Chem Soc*, 2017, 139: 1885–1893

108 Kuhn AN, Zhao H, Nwabara UO, Lu X, Liu M, Pan Y-, Zhu W, Kenis PJA, Yang H. *Adv Funct Mater*, 2021, 31: 2101668

109 Wang P, Yang H, Xu Y, Huang X, Wang J, Zhong M, Cheng T, Shao Q. *ACS Nano*, 2021, 15: 1039–1047

110 Zhong Y, Kong X, Song Z, Liu Y, Peng L, Zhang L, Luo X, Zeng J, Geng Z. *Nano Lett*, 2022, 22: 2554–2560

111 Shang L, Lv X, Shen H, Shao Z, Zheng G. *J Colloid Interface Sci*, 2019, 552: 426–431

112 Liang ZQ, Zhuang TT, Seifitokaldani A, Li J, Huang CW, Tan CS, Li Y, De Luna P, Dinh CT, Hu Y, Xiao Q, Hsieh PL, Wang Y, Li F, Quintero-Bermudez R, Zhou Y, Chen P, Pang Y, Lo SC, Chen LJ, Tan H, Xu Z, Zhao S, Sinton D, Sargent EH. *Nat Commun*, 2018, 9: 3828

113 Zhuang TT, Liang ZQ, Seifitokaldani A, Li Y, De Luna P, Burdyny T, Che F, Meng F, Min Y, Quintero-Bermudez R, Dinh CT, Pang Y, Zhong M, Zhang B, Li J, Chen PN, Zheng XL, Liang H, Ge WN, Ye BJ, Sinton D, Yu SH, Sargent EH. *Nat Catal*, 2018, 1: 421–428

114 Nitopi S, Bertheussen E, Scott SB, Liu X, Engstfeld AK, Horch S, Seger B, Stephens IEL, Chan K, Hahn C, Nørskov JK, Jaramillo TF, Chorkendorff I. *Chem Rev*, 2019, 119: 7610–7672

115 Tan D, Zhang J, Cheng X, Tan X, Shi J, Zhang B, Han B, Zheng L, Zhang J. *Chem Sci*, 2019, 10: 4491–4496

116 Mistry H, Reske R, Strasser P, Roldan Cuenya B. *Catal Today*, 2017, 288: 30–36

117 Zhong M, Tran K, Min Y, Wang C, Wang Z, Dinh CT, De Luna P, Yu Z, Rasouli AS, Brodersen P, Sun S, Voznyy O, Tan CS, Askerka M, Che F, Liu M, Seifitokaldani A, Pang Y, Lo SC, Ip A, Ulissi Z, Sargent EH. *Nature*, 2020, 581: 178–183

118 Yang CL, Wang LN, Yin P, Liu J, Chen MX, Yan QQ, Wang ZS, Xu SL, Chu SQ, Cui C, Ju H, Zhu J, Lin Y, Shui J, Liang HW. *Science*, 2021, 374: 459–464

119 Kim D, Xie C, Becknell N, Yu Y, Karamad M, Chan K, Crumlin EJ, Nørskov JK, Yang P. *J Am Chem Soc*, 2017, 139: 8329–8336

120 Li M, Song N, Luo W, Chen J, Jiang W, Yang J. *Adv Sci*, 2022, 10: 2204579

121 Hoffman ZB, Gray TS, Moraveck KB, Gunnoe TB, Zangari G. *ACS Catal*, 2017, 7: 5381–5390

122 Katoh A, Uchida H, Shibata M, Watanabe M. *J Electrochem Soc*, 1994, 141: 2054–2058

123 Li X, Wu X, Lv X, Wang J, Wu HB. *Chem Catal*, 2022, 2: 262–291

124 Back S, Kim JH, Kim YT, Jung Y. *ACS Appl Mater Interfaces*, 2016, 8: 23022–23027

125 Wu Z, Wu H, Cai W, Wen Z, Jia B, Wang L, Jin W, Ma T. *Angew Chem Int Ed*, 2021, 60: 12554–12559

126 Wang J, Zou J, Hu X, Ning S, Wang X, Kang X, Chen S. *J Mater Chem A*, 2019, 7: 27514–27521

127 Han X, Mou T, Liu S, Ji M, Gao Q, He Q, Xin H, Zhu H. *Nanoscale Horiz*, 2022, 7: 508–514

128 Wang P, Qiao M, Shao Q, Pi Y, Zhu X, Li Y, Huang X. *Nat Commun*, 2018, 9: 4933

129 Gao D, Zhang Y, Zhou Z, Cai F, Zhao X, Huang W, Li Y, Zhu J, Liu P, Yang F, Wang G, Bao X. *J Am Chem Soc*, 2017, 139: 5652–5655

130 Wang C, Pang R, Pan Z, Zhu Y, Li C, Liu B, Shen J. *J Mater Chem A*, 2022, 10: 22694–22700

131 Yan X, Chen C, Wu Y, Liu S, Chen Y, Feng R, Zhang J, Han B. *Chem Sci*, 2021, 12: 6638–6645

132 Chu S, Yan X, Choi C, Hong S, Robertson AW, Masa J, Han B, Jung Y, Sun Z. *Green Chem*, 2020, 22: 6540–6546

133 Zhao Z, Li X, Wang J, Lv X, Wu HB. *J CO2 Utilization*, 2021, 54: 101741

134 Li H, Yu P, Lei R, Yang F, Wen P, Ma X, Zeng G, Guo J, Toma FM, Qiu Y, Geyer SM, Wang X, Cheng T, Drisdell WS. *Angew Chem Int Ed*, 2021, 60: 24838–24843

135 Sultan S, Lee H, Park S, Kim MM, Yoon A, Choi H, Kong TH, Koe YJ, Oh HS, Lee Z, Kim H, Kim W, Kwon Y. *Energy Environ Sci*, 2022, 15: 2397–2409

136 Li X, Wang J, Lv X, Yang Y, Xu Y, Liu Q, Wu HB. *Nano-Micro Lett*, 2022, 14: 134

137 Li X, Liu Q, Wang J, Meng D, Shu Y, Lv X, Zhao B, Yang H, Cheng T, Gao Q, Li L, Wu HB. *Chem*, 2022, 8: 2148–2162

138 Hannagan RT, Giannakakis G, Flytzani-Stephanopoulos M, Sykes ECH. *Chem Rev*, 2020, 120: 12044–12088

139 Kyriakou G, Boucher MB, Jewell AD, Lewis EA, Lawton TJ, Baber AE, Tierney HL, Flytzani-Stephanopoulos M, Sykes ECH. *Science*, 2012, 335: 1209–1212

140 Greiner MT, Jones TE, Beeg S, Zwiener L, Scherzer M, Girgsdies F, Piccinin S, Armbrüster M, Knop-Gericke A, Schlögl R. *Nat Chem*, 2018, 10: 1008–1015

141 Zhao Z, Lu G. *J Phys Chem C*, 2019, 123: 4380–4387

142 Cheng MJ, Clark EL, Pham HH, Bell AT, Head-Gordon M. *ACS Catal*, 2016, 6: 7769–7777

143 Zheng T, Liu C, Guo C, Zhang M, Li X, Jiang Q, Xue W, Li H, Li A, Pao CW, Xiao J, Xia C, Zeng J. *Nat Nanotechnol*, 2021, 16: 1386–1393

144 Zhang M, Zhang Z, Zhao Z, Huang H, Anjum DH, Wang D, He J, Huang KW. *ACS Catal*, 2021, 11: 11103–11108

145 Yang S, Liu Z, An H, Arnouts S, de Ruiter J, Rollier F, Bals S, Altantzis T, Figueiredo MC, Filot IAW, Hensen EJM, Weckhuysen BM, van der Stam W. *ACS Catal*, 2022, 12: 15146–15156

146 Ren W, Tan X, Qu J, Li S, Li J, Liu X, Ringer SP, Cairney JM, Wang K, Smith SC, Zhao C. *Nat Commun*, 2021, 12: 1449

147 Li K, Xu J, Zheng T, Yuan Y, Liu S, Shen C, Jiang T, Sun J, Liu Z, Xu Y, Chuai M, Xia C, Chen W. *ACS Catal*, 2022, 12: 9922–9932

148 Song X, Xu L, Sun X, Han B. *Sci China Chem*, 2023, 66: 315–323

149 Ye K, Zhou Z, Shao J, Lin L, Gao D, Ta N, Si R, Wang G, Bao X. *Angew Chem Int Ed*, 2020, 59: 4814–4821

150 Herzog A, Bergmann A, Jeon HS, Timoshenko J, Kühl S, Rettenmaier C, Lopez Luna M, Haase FT, Roldan Cuenya B. *Angew Chem Int Ed*, 2021, 60: 7426–7435

151 Gao D, Zhou H, Cai F, Wang J, Wang G, Bao X. *ACS Catal*, 2018, 8: 1510–1519

152 Gao D, Zhou H, Cai F, Wang D, Hu Y, Jiang B, Cai WB, Chen X, Si R, Yang F, Miao S, Wang J, Wang G, Bao X. *Nano Res*, 2017, 10: 2181–2191

153 Lin R, Ma X, Cheong WC, Zhang C, Zhu W, Pei J, Zhang K, Wang B, Liang S, Liu Y, Zhuang Z, Yu R, Xiao H, Li J, Wang D, Peng Q, Chen C, Li Y. *Nano Res*, 2019, 12: 2866–2871

154 Bagger A, Ju W, Varela AS, Strasser P, Rossmeisl J. *ChemPhysChem*, 2017, 18: 3266–3273

155 Kottakkat T, Klingan K, Jiang S, Jovanov ZP, Davies VH, El-Nagar GAM, Dau H, Roth C. *ACS Appl Mater Interfaces*, 2019, 11: 14734–14744

156 Iyengar P, Kolb MJ, Pankhurst J, Calle-Vallejo F, Buonsanti R. *ACS*

Catal, 2021, 11: 13330–13336

157 Pardo Pérez LC, Arndt A, Stojkovikj S, Ahmet IY, Arens JT, Dattila F, Wendt R, Guilherme Buzanich A, Radtke M, Davies V, Höflich K, Köhnen E, Tockhorn P, Golnak R, Xiao J, Schuck G, Wollgarten M, López N, Mayer MT. *Adv Energy Mater*, 2022, 12: 2103328

158 Choi YW, Scholten F, Sinev I, Roldan Cuenya B. *J Am Chem Soc*, 2019, 141: 5261–5266

159 Huo S, Weng Z, Wu Z, Zhong Y, Wu Y, Fang J, Wang H. *ACS Appl Mater Interfaces*, 2017, 9: 28519–28526

160 Ismail AM, Csapó E, Janáky C. *Electrochim Acta*, 2019, 313: 171–178

161 Yu Q, Meng X, Shi L, Liu H, Ye J. *Chem Commun*, 2016, 52: 14105–14108

162 Zhang Z, Wen G, Luo D, Ren B, Zhu Y, Gao R, Dou H, Sun G, Feng M, Bai Z, Yu A, Chen Z. *J Am Chem Soc*, 2021, 143: 6855–6864

163 Choi J, Kim MJ, Ahn SH, Choi I, Jang JH, Ham YS, Kim JJ, Kim SK. *Chem Eng J*, 2016, 299: 37–44

164 Lee H, Kim SK, Ahn SH. *J Industrial Eng Chem*, 2017, 54: 218–225

165 Xu Z, Lai E, Shao-Horn Y, Hamad-Schifferli K. *Chem Commun*, 2012, 48: 5626–5628

166 Hu H, Tang Y, Hu Q, Wan P, Dai L, Yang XJ. *Appl Surf Sci*, 2018, 445: 281–286

167 Andrews E, Fang Y, Flake J. *J Appl Electrochem*, 2018, 48: 435–441

168 Chen K, Zhang X, Williams T, Bourgeois L, MacFarlane DR. *Electrochim Acta*, 2017, 239: 84–89

169 Lamaison S, Wakerley D, Montero D, Rousse G, Taverna D, Giaume D, Mercier D, Blanchard J, Tran HN, Fontecave M, Mougel V. *ChemSusChem*, 2019, 12: 511–517

170 Hirunsit P. *J Phys Chem C*, 2013, 117: 8262–8268

171 Christophe J, Doneux T, Buess-Herman C. *Electrocatalysis*, 2012, 3: 139–146

172 Jedidi A, Rasul S, Masih D, Cavallo L, Takanabe K. *J Mater Chem A*, 2015, 3: 19085–19092

173 Rasul S, Anjum DH, Jedidi A, Minenkov Y, Cavallo L, Takanabe K. *Angew Chem Int Ed*, 2015, 54: 2146–2150

174 Larrazábal GO, Martín AJ, Mitchell S, Hauert R, Pérez-Ramírez J. *ACS Catal*, 2016, 6: 6265–6274

175 Zhao Y, Wang C, Wallace GG. *J Mater Chem A*, 2016, 4: 10710–10718

176 Schreier M, Héroguel F, Steier L, Ahmad S, Luterbacher JS, Mayer MT, Luo J, Grätzel M. *Nat Energy*, 2017, 2: 17087

177 Zeng J, Bejtka K, Ju W, Castellino M, Chiodoni A, Sacco A, Far-khondehfal MA, Hernández S, Rentsch D, Battaglia C, Pirri CF. *Appl Catal B-Environ*, 2018, 236: 475–482

178 Ju W, Zeng J, Bejtka K, Ma H, Rentsch D, Castellino M, Sacco A, Pirri CF, Battaglia C. *ACS Appl Energy Mater*, 2019, 2: 867–872

179 Ju W, Jiang F, Ma H, Pan Z, Zhao Y-, Pagani F, Rentsch D, Wang J, Battaglia C. *Adv Energy Mater*, 2019, 9: 1901514

180 Gao J, Li J, Liu Y, Xia M, Finfrock YZ, Zakeeruddin SM, Ren D, Grätzel M. *Nat Commun*, 2022, 13: 5898

181 Zhu S, Wang Q, Qin X, Gu M, Tao R, Lee BP, Zhang L, Yao Y, Li T, Shao M. *Adv Energy Mater*, 2018, 8: 1802238

182 Valenti M, Prasad NP, Kas R, Bohra D, Ma M, Balasubramanian V, Chu L, Gimenez S, Bisquert J, Dam B, Smith WA. *ACS Catal*, 2019, 9: 3527–3536

183 Hou Y, Erni R, Widmer R, Rahaman M, Guo H, Fasel R, Moreno-García P, Zhang Y, Broekmann P. *ChemElectroChem*, 2019, 6: 3189–3198

184 Mun Y, Lee S, Cho A, Kim S, Han JW, Lee J. *Appl Catal B-Environ*, 2019, 246: 82–88

185 Wen G, Lee DU, Ren B, Hassan FM, Jiang G, Cano ZP, Gostick J, Croiset E, Bai Z, Yang L, Chen Z. *Adv Energy Mater*, 2018, 8: 1802427

186 Tang J, Daiyan R, Ghasemian MB, Idrus-Saidi SA, Zavabeti A, Daeneke T, Yang J, Koshy P, Cheong S, Tilley RD, Kaner RB, Amal R, Kalantar-Zadeh K. *Nat Commun*, 2019, 10: 4645

187 Yuan T, Hu Z, Zhao Y, Fang J, Lv J, Zhang Q, Zhuang Z, Gu L, Hu S. *Nano Lett*, 2020, 20: 2916–2922

188 Lai Q, Yang N, Yuan G. *Electrochem Commun*, 2017, 83: 24–27

189 Choi SY, Jeong SK, Kim HJ, Baek IH, Park KT. *ACS Sustain Chem Eng*, 2016, 4: 1311–1318

190 Dong WJ, Yoo CJ, Lee JL. *ACS Appl Mater Interfaces*, 2017, 9: 43575–43582

191 Hailu A, Tamijani AA, Mason SE, Shaw SK. *Energy Fuels*, 2020, 34: 3467–3476

192 Zhang X, Li F, Zhang Y, Bond AM, Zhang J. *J Mater Chem A*, 2018, 6: 7851–7858

193 Jia L, Yang H, Deng J, Chen J, Zhou Y, Ding P, Li L, Han N, Li Y. *Chin J Chem*, 2019, 37: 497–500

194 Zu MY, Zhang L, Wang C, Zheng LR, Yang HG. *J Mater Chem A*, 2018, 6: 16804–16809

195 Ye K, Cao A, Shao J, Wang G, Si R, Ta N, Xiao J, Wang G. *Sci Bull*, 2020, 65: 711–719

196 Peng L, Wang Y, Masood I, Zhou B, Wang Y, Lin J, Qiao J, Zhang FY. *Appl Catal B-Environ*, 2020, 264: 118447

197 Hou X, Cai Y, Zhang D, Li L, Zhang X, Zhu Z, Peng L, Liu Y, Qiao J. *J Mater Chem A*, 2019, 7: 3197–3205

198 Wang X, Fei X, Wang M, Wang W, Yang Z, Ning H, Zhang Y, Wang L, Jin X, Wu M. *J Mater Chem A*, 2022, 10: 23542–23550

199 Lu X, Wu Y, Yuan X, Wang H. *Angew Chem Int Ed*, 2019, 58: 4031–4035

200 Bai X, Chen W, Zhao C, Li S, Song Y, Ge R, Wei W, Sun Y. *Angew Chem Int Ed*, 2017, 56: 12219–12223

201 Lv H, Lv F, Qin H, Min X, Sun L, Han N, Xu D, Li Y, Liu B. *CCS Chem*, 2022, 4: 1376–1385

202 Karamad M, Tripkovic V, Rossmeisl J. *ACS Catal*, 2014, 4: 2268–2273

203 Wang X, Lv J, Zhang J, Wang XL, Xue C, Bian G, Li D, Wang Y, Wu T. *Nanoscale*, 2020, 12: 772–784

204 Yoo JS, Christensen R, Vegge T, Nørskov JK, Studt F. *ChemSusChem*, 2016, 9: 358–363

205 Zheng X, Ji Y, Tang J, Wang J, Liu B, Steinrück HG, Lim K, Li Y, Toney MF, Chan K, Cui Y. *Nat Catal*, 2019, 2: 55–61

206 Zhang S, Zhao S, Qu D, Liu X, Wu Y, Chen Y, Huang W. *Small*, 2021, 17: 2102293

207 Hoang TTH, Verma S, Ma S, Fister TT, Timoshenko J, Frenkel AI, Kenis PJA, Gewirth AA. *J Am Chem Soc*, 2018, 140: 5791–5797

208 Yang C, Ko BH, Hwang S, Liu Z, Yao Y, Luc W, Cui M, Malkani AS, Li T, Wang X, Dai J, Xu B, Wang G, Su D, Jiao F, Hu L. *Sci Adv*, 2020, 6: eaaz6844

209 Xie Y, Ou P, Wang X, Xu Z, Li YC, Wang Z, Huang JE, Wicks J, McCallum C, Wang N, Wang Y, Chen T, Lo BTW, Sinton D, Yu JC, Wang Y, Sargent EH. *Nat Catal*, 2022, 5: 564–570

210 Guo X, Zhang Y, Deng C, Li X, Xue Y, Yan YM, Sun K. *Chem Commun*, 2015, 51: 1345–1348

211 Kibria MG, Edwards JP, Gabardo CM, Dinh CT, Seifitokaldani A, Sinton D, Sargent EH. *Adv Mater*, 2019, 31: 1807166

212 Liu W, Zhai P, Li A, Wei B, Si K, Wei Y, Wang X, Zhu G, Chen Q, Gu X, Zhang R, Zhou W, Gong Y. *Nat Commun*, 2022, 13: 1877

213 Shen S, Peng X, Song L, Qiu Y, Li C, Zhuo L, He J, Ren J, Liu X, Luo J. *Small*, 2019, 15: 1902229

214 Peterson AA, Abild-Pedersen F, Studt F, Rossmeisl J, Nørskov JK. *Energy Environ Sci*, 2010, 3: 1311–1315

215 Nie X, Esopi MR, Janik MJ, Asthagiri A. *Angew Chem Int Ed*, 2013, 52: 2459–2462

216 Andrews E, Ren M, Wang F, Zhang Z, Sprunger P, Kurtz R, Flake J. *J Electrochem Soc*, 2013, 160: H841–H846

217 Ledezma-Yanez I, Gallent EP, Koper MTM, Calle-Vallejo F. *Catal Today*, 2016, 262: 90–94

218 Cheng T, Xiao H, Goddard Iii WA. *Proc Natl Acad Sci USA*, 2017, 114: 1795–1800

219 Lum Y, Cheng T, Goddard Iii WA, Ager JW. *J Am Chem Soc*, 2018, 140: 9337–9340

220 Hori Y, Murata A, Takahashi R. *J Chem Soc Faraday Trans 1*, 1989,

85: 2309–2326

221 Ma S, Sadakiyo M, Luo R, Heima M, Yamauchi M, Kenis PJA. *J Power Sources*, 2016, 301: 219–228

222 Zhong J, Yang X, Wu Z, Liang B, Huang Y, Zhang T. *Chem Soc Rev*, 2020, 49: 1385–1413

223 Lv X, Shang L, Zhou S, Li S, Wang Y, Wang Z, Sham T-, Peng C, Zheng G. *Adv Energy Mater*, 2020, 10: 2001987

224 Jia F, Yu X, Zhang L. *J Power Sources*, 2014, 252: 85–89

225 Zhu W, Zhao K, Liu S, Liu M, Peng F, An P, Qin B, Zhou H, Li H, He Z. *J Energy Chem*, 2019, 37: 176–182

226 Lu L, Sun X, Ma J, Yang D, Wu H, Zhang B, Zhang J, Han B. *Angew Chem Int Ed*, 2018, 57: 14149–14153

227 Shang L, Lv X, Zhong L, Li S, Zheng G. *Small Methods*, 2022, 6: 2101334

228 Wang X, Wang Z, García de Arquer FP, Dinh CT, Ozden A, Li YC, Nam DH, Li J, Liu YS, Wicks J, Chen Z, Chi M, Chen B, Wang Y, Tam J, Howe JY, Proppe A, Todorović P, Li F, Zhuang TT, Gabardo CM, Kirmani AR, McCallum C, Hung SF, Lum Y, Luo M, Min Y, Xu A, O'Brien CP, Stephen B, Sun B, Ip AH, Richter LJ, Kelley SO, Sinton D, Sargent EH. *Nat Energy*, 2020, 5: 478–486

229 Wang P, Yang H, Tang C, Wu Y, Zheng Y, Cheng T, Davey K, Huang X, Qiao SZ. *Nat Commun*, 2022, 13: 3754

230 Gurudayal , Perone D, Malani S, Lum Y, Haussener S, Ager JW. *ACS Appl Energy Mater*, 2019, 2: 4551–4559

231 Ting LRL, Piqué O, Lim SY, Tanhaei M, Calle-Vallejo F, Yeo BS. *ACS Catal*, 2020, 10: 4059–4069

232 Chang CJ, Hung SF, Hsu CS, Chen HC, Lin SC, Liao YF, Chen HM. *ACS Cent Sci*, 2019, 5: 1998–2009

233 Ren D, Gao J, Pan L, Wang Z, Luo J, Zakeeruddin SM, Hagfeldt A, Grätzel M. *Angew Chem Int Ed*, 2019, 58: 15036–15040

234 Hu F, Yang L, Jiang Y, Duan C, Wang X, Zeng L, Lv X, Duan D, Liu Q, Kong T, Jiang J, Long R, Xiong Y. *Angew Chem Int Ed*, 2021, 60: 26122–26127

235 Fu J, Zhu W, Chen Y, Yin Z, Li Y, Liu J, Zhang H, Zhu J-, Sun S. *Angew Chem Int Ed*, 2019, 58: 14100–14103

236 Tao Z, Wu Z, Yuan X, Wu Y, Wang H. *ACS Catal*, 2019, 9: 10894–10898

237 Wang H, Zhou X, Yu T, Lu X, Qian L, Liu P, Lei P. *Electrochim Acta*, 2022, 426: 140774

238 Wang W, Wang Z, Yang R, Duan J, Liu Y, Nie A, Li H, Xia BY, Zhai T. *Angew Chem Int Ed*, 2021, 60: 22940–22947

239 Zhang S, Kang P, Bakir M, Lapides AM, Dares CJ, Meyer TJ. *Proc Natl Acad Sci USA*, 2015, 112: 15809–15814

240 Zhang H, Wang C, Luo H, Chen J, Kuang M, Yang J. *Angew Chem Int Ed*, 2023, 62: e202217071

241 Xie M, Shen Y, Ma W, Wei D, Zhang B, Wang Z, Wang Y, Zhang Q, Xie S, Wang C, Wang Y. *Angew Chem Int Ed*, 2022, 61: e202213423

242 Torelli DA, Francis SA, Crompton JC, Javier A, Thompson JR, Brunschwig BS, Soriaga MP, Lewis NS. *ACS Catal*, 2016, 6: 2100–2104

243 Paris AR, Bocarsly AB. *ACS Catal*, 2017, 7: 6815–6820

244 Frese KW, Canfield D. *J Electrochem Soc*, 1984, 131: 2518–2522

245 Zhang Q, Tao S, Du J, He A, Yang Y, Tao C. *J Mater Chem A*, 2020, 8: 8410–8420

246 He J, Dettelbach KE, Huang A, Berlinguette CP. *Angew Chem Int Ed*, 2017, 56: 16579–16582

247 Li K, Chen W. *Mater Today Energy*, 2021, 20: 100638

248 Nellaiappan S, Katiyar NK, Kumar R, Parui A, Malviya KD, Pradeep KG, Singh AK, Sharma S, Tiwary CS, Biswas K. *ACS Catal*, 2020, 10: 3658–3663

249 Pedersen JK, Batchelor TAA, Bagger A, Rossmeisl J. *ACS Catal*, 2020, 10: 2169–2176

250 Li H, Huang H, Chen Y, Lai F, Fu H, Zhang L, Zhang N, Bai S, Liu T. *Adv Mater*, 2022, 35: 2209242

251 He J, Dettelbach KE, Salvatore DA, Li T, Berlinguette CP. *Angew Chem Int Ed*, 2017, 56: 6068–6072

252 Yuan Q, Yang H, Xie M, Cheng T. *Acta Physico Chim Sin*, 2020, 0: 2010040–0

253 Yang Z, Gao W, Jiang Q. *J Mater Chem A*, 2020, 8: 17507–17515

254 Tran K, Ulissi ZW. *Nat Catal*, 2018, 1: 696–703

255 Ma X, Li Z, Achenie LEK, Xin H. *J Phys Chem Lett*, 2015, 6: 3528–3533